Water Resources Research

RESEARCH ARTICLE
10.1029/2022WR034151

Influence of Bed Roughness on Flow and Turbulence Structure Around a Partially-Buried, Isolated Freshwater Mussel

T. Lazzarin[1], G. Constantinescu[2], L. Di Micco[1], H. Wu[2], F. Lavignani[3], M. Lo Brutto[3], D. Termini[3,4], and D. P. Viero[1]

[1]Department of Civil, Environmental and Architectural Engineering, University of Padova, Padova, Italy, [2]Department of Civil and Environmental Engineering and IIHR-Hydroscience and Engineering, University of Iowa, Iowa City, IA, USA, [3]Department of Engineering, University of Palermo, Palermo, Italy, [4]NBFC, National Biodiversity Future Center, Palermo, Italy

Key Points:

- Numerical simulations resolving flow and eddies over a gravel bed and past a partially-buried freshwater mussel
- The effects of varying the burial level of the mussel, the discharge through the two mussel siphons, and the bed-roughness height are investigated
- Increasing the bed roughness produces significant differences in the flow field, turbulence structure, and drag force compared to a smooth bed

Correspondence to:
D. P. Viero,
daniele.viero@unipd.it

Citation:
Lazzarin, T., Constantinescu, G., Di Micco, L., Wu, H., Lavignani, F., Lo Brutto, M., et al. (2023). Influence of bed roughness on flow and turbulence structure around a partially-buried, isolated freshwater mussel. *Water Resources Research*, *59*, e2022WR034151. https://doi.org/10.1029/2022WR034151

Received 22 NOV 2022
Accepted 11 APR 2023

Author Contributions:
Conceptualization: G. Constantinescu, D. P. Viero
Data curation: L. Di Micco, F. Lavignani
Formal analysis: T. Lazzarin
Funding acquisition: D. Termini, D. P. Viero
Investigation: T. Lazzarin, M. Lo Brutto
Methodology: T. Lazzarin, G. Constantinescu, L. Di Micco, H. Wu
Project Administration: D. P. Viero
Supervision: G. Constantinescu, D. Termini, D. P. Viero
Validation: L. Di Micco, H. Wu
Visualization: T. Lazzarin
Writing – original draft: T. Lazzarin
Writing – review & editing: G. Constantinescu, D. Termini, D. P. Viero

Abstract The present study uses eddy-resolving numerical simulations to investigate how bed roughness affects flow and turbulence structure around an isolated, partially-buried mussel (*Unio elongatulus*) aligned with the incoming flow. The rough-bed simulations resolve the flow past the exposed part of a gravel bed, whose surface is obtained from a laboratory experiment that also provides some additional data for validation of the numerical model. Results are also discussed for the limiting case of a horizontal smooth bed. Additionally, the effects of varying the level of burial of the mussel inside the substrate and the discharge through the two mussel siphons are investigated via a set of simulations in which the ratio between the median diameter of the (gravel) particles forming the rough bed, d_{50}, and the height of the exposed part of the mussel, h, varies between 0.10 and 0.22. The increase of the bed roughness is associated with a strong amplification of the turbulence kinetic energy in the near-wake region. Increasing the bed roughness and/or reducing h intensifies the interactions of the eddies generated by the bed particles with the base and tip vortices induced by the active filtering and by the mussel shell, respectively, which, in turn, induces a more rapid dissipation of these vortices. Increasing the bed roughness also reduces the strength of the main downwelling flow region forming in the wake. The strong downwelling near the symmetry plane is the main reason why the symmetric wake shedding mode dominates in the smooth bed simulations with negligible active filtering. By contrast, the anti-symmetric wake shedding mode dominates in the simulations conduced with a high value of the bed roughness. The mean streamwise drag force coefficient for the emerged part of the shell and the dilution of the excurrent siphon jet increase with increasing bed roughness.

1. Introduction

Freshwater mussels are molluscs that live at the sediment–water interface. They are often encountered in sand and gravel bed rivers that provide more favorable habitat. They play an important role in many fluvial environments by increasing the sustainability of stream ecosystems (Marion et al., 2014). For example, they constitute a fundamental link in many food chains (Howard & Cufey, 2006; Vaughn et al., 2004, 2008), contribute to the filtration of suspended material (Hajisafarali et al., 2022; Kreeger et al., 2018), provide habitat for fish and insects (Gutiérrez et al., 2003) and can be used as bioindicators for water quality (Doucet et al., 2021; Haag, 2012). A full understanding of the ecological roles played by mussels requires an interdisciplinary approach involving ecological, biomechanical and environmental fluid mechanics research tools (Nikora, 2010).

The shell of a mussel is composed by two valves that are slightly asymmetric with respect to a central axis. In the lower part of the mussel, a foot allows the mollusk to be anchored at the bed and to move slowly, both horizontally and vertically. In particular, mussels react to the incoming flow by assuming an orientation which is parallel to the incoming flow direction to minimize drag forces on the shell (Di Maio & Corkum, 1997). For most mussels anchored into the substrate, the foot is usually situated below the mean bed level and the shell is partially buried. The mussel has two siphons to acquire nutrients from the surrounding environment. The incurrent, or inhaling, siphon is typically oriented upstream and organic particles, such as plankton, enter the mollusk's body via this siphon. The excurrent, or exhaling, siphon is also positioned upstream but oriented upwards. Through it, a jet of filtered water (e.g., with very low concentrations of nutrients, waste, and dissolved organic matter) is reintroduced in the channel (Kumar et al., 2019; O'Riordan et al., 1995; Perles et al., 2003). Mussels are a major contributor to purifying water in rivers. The filtering rate has been measured experimentally (Kryger & Riisgård, 1988;

Monismith et al., 1990; Nishizaki & Ackerman, 2017) and it was shown to be dependent on the mussel species and dimensions (Bunt et al., 1993). Mussels can modify their filtering rates and level of burial to adapt to changing flow conditions. Mussels play other important roles for the river ecosystem. For example, they provide suitable habitat for benthic organisms and increase bed stability especially in gravel-bed rivers (Lohrer et al., 2004).

Freshwater mussels are among the world's most imperiled fauna (Ferreira-Rodríguez et al., 2019; Lydeard et al., 2004; Strayer et al., 2004). The survival of the mussel is strongly dependent on the aquatic environment in which they live (Lopez et al., 2022). Together with the chemical and biological characteristics of the habitat (e.g., availability of nutrients, water pH and temperature), flow hydrodynamics plays an important role for mollusk conservation efforts as it influences habitat conditions. To a large measure, conserving freshwater mussel communities is dependent on understanding the hydrodynamic responses of freshwater mussels and creating favorable habitats that can sustain mussel populations over long periods of time (Blettler et al., 2010; Engelhardt et al., 2004; Nakato et al., 2007; Zigler et al., 2008). There are still important gaps in understanding how mussels interact with the surrounding habitat at the organism-level scale (Lopez & Vaughn, 2021).

Mussels are known to be very sensitive to mean shear stresses in the river reach (Modesto et al., 2023; Morales et al., 2006; Strayer, 1999). In particular, mussels have a much higher probability to survive high flow events if situated in regions of low bed shear stress (Newton et al., 2008). High bed shear stresses can entrain sediment from the bed surface and induce local scour around the shell, which can lead to the mussel being dislocated from the substrate. High bed shear stresses generally correlate with high drag forces acting on the emerged part of the shell, which can also lead to mussel dislocation. These mechanisms leading to mussel dislocation are particularly relevant during floods when not only the average values of the bed shear stress and drag forces increase, but also the instantaneous values are subject to much larger variations with respect to the mean values. For this reason, floods and extreme events are recognized to be one of the first causes threatening mussel conservation (Sansom et al., 2018).

The generation of larger-scale turbulence and high values of turbulent kinetic energy around the mussels may also affect the quality of the habitat and, ultimately, the capacity of the mussel to survive (Rehmann et al., 2003). Together with macro-scale hydrodynamics patterns, local turbulent structures also affect the overall capacity of the overflow to dislocate mussels from the bed. The mussel shell constitutes a surface-mounted obstacle, increasing velocity and shear stress on the sides of the mussel, and producing a recirculation region behind the shell. The diversion of the incoming flow by the emerged part of the mussel generates energetic vortical structures which interact with the large-scale coherent structures generated over a rough bed (e.g., super-streaks and eddies generated in the separated shear layers forming at the top of the larger bed roughness elements, see K. Chang & Constantinescu, 2013). Some of these eddies (e.g., horseshoe vortices, wake vortices, vortex tubes in the separated shear layers, longitudinal base and tip vortices in the near wake) are situated, or are advected, in the vicinity of the bed surface. Their presence and/or their passage can result in a large amplification of the instantaneous bed shear stresses and forces acting on the mussel.

Freshwater mussels can live on gravel beds whose roughness is relatively high since coarse substrates enhance both bed stability and water mixing, which are key aspects of mussel habitats. The mean sediment size (e.g., as quantified by the d_{50} and d_{90} diameters) of the bed particles can be as high as 10% of the height of the emerged part of the mussel, h. The particles situated at the surface of a rough bed in turbulent flow generate energetic eddies which increase the turbulence kinetic energy (TKE) close to the bed surface compared to typical values observed over a smooth bed at the same channel Reynolds number. These effects are even higher for river beds containing graded sediments where sediment particles that are much larger compared to the average bed particle size are present at some locations. These particles act as local large-scale roughness elements, similar to the emerged parts of the mussel shell. Eddies generated by the large bed particles situated upstream of the mussel significantly alter the local flow field near the mussel and interact with the turbulent structures generated by the shell itself. This affects both the instantaneous and mean bed shear stresses around the mussel and the drag forces acting on the emerged part of the mussel which control mussel stability.

Several numerical studies that resolve the dynamically important coherent structures in the flow were conducted for an isolated mussel, or a small cluster of partially-burrowed mussels, placed on a horizontal, smooth bed. These studies provided lots of information on the type of vortical structures generated by partially-burrowed mussels, their dynamics and their effects on the drag forces and capacity of the flow to induce local scour as a function of the exposed height of the mussel, the direction of the incoming flow relative to the major axis of the

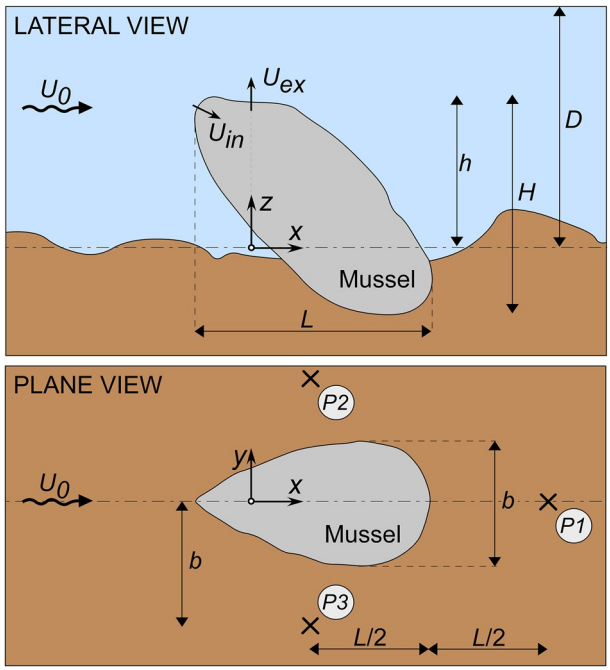

Figure 1. Sketch of the mussel shell. U_0 is the section-averaged velocity in the channel, L, H, and b are the mussel's length, height and width in the x, y, z reference frame, respectively (the position $z = 0$ identifies the mean bed elevation), h is the height of the exposed part, U_{in} and U_{ex} are the mean velocities through the incurrent and the excurrent siphons, respectively, and D is the height of the water column above the bed. $P1$, $P2$, $P3$ are the horizontal locations where vertical profiles of the streamwise velocity were measured experimentally (see Section 2.5).

mussel and the strength of the filtering flow (Constantinescu et al., 2013; H. Wu & Constantinescu, 2022; H. Wu, Constantinescu, & Zeng, 2020). To the best of our knowledge, eddy resolving techniques were not yet used to provide a similar description of the flow and turbulence structure around a mussel placed on a rough bed that approximates a natural benthic environment and of the dynamics of the larger-scale coherent structures that control the capacity of the flow to induce local scour and mixing between the filtered water entering the channel through the excurrent siphon and the surrounding flow. In the case of experimental studies conducted in the lab, information on the mean flow and turbulence variables (*TKE*, Reynolds stresses) is generally available in a limited number of sections and/or a limited number of horizontal locations around the mussel (Crimaldi et al., 2002; Kumar et al., 2019; Sansom et al., 2018). This includes laboratory studies conducted for surface-mounted obstacles of simpler shapes (e.g., semi-ellipsoids) that are relatively similar to that of a partially-burrowed mussel (e.g., see Hajimirzaie & Buchholz, 2013; Hajimirzaie et al., 2012). Moreover, the latter type of studies was only conducted for channels with a smooth horizontal bed and without accounting for the siphonal flows.

Eddy resolving techniques are a powerful tool to provide critical information on the dynamics of the large-scale turbulence given the complex, three-dimensional shapes of most of the dynamically important eddies in the flow investigated here (Keylock et al., 2005, 2012). For such cases, information collected in two-dimensional (2-D) planes is not sufficient to describe the vortical structure of the flow, the interaction of these coherent structures with the bed and mussel surface and their role in transport and mixing processes. On the other hand, for eddy resolving simulations to model in a realistic way the generation of turbulent eddies by a rough bed and the interactions of these eddies with the mussel's shell, the simulation needs to resolve the flow over the individual roughness elements forming the rough bed surface rather than simply account for the bed roughness via an empirical roughness model (H. Wu et al., 2021). This is the approach followed in the present study, where a gravel bed surface is obtained from a flume experiment conducted as part of a larger research program.

The present study uses a species of freshwater mussels (*Unio elongatulus*) that is characterized by a more streamlined body compared to the mussel (*L. siliquoidea*) used by H. Wu, Constantinescu, and Zeng (2020) and H. Wu and Constantinescu (2022) in their smooth bed simulations of flow past partially-burrowed mussels. Moreover, the *Unio elongatulus* mussel tends to present large differences between the front side and its back side such that the (top of the) mussel appears to be inclined toward the incoming flow (Figure 1). This is different from the *L. siliquoidea* mussels whose shell is more symmetrical and much less tilted toward the incoming flow. Given that mussel beds tend to be more common in gravel bed rivers, understanding flow structure for a partially-burrowed mussel placed on a rough bed is of particular interest for efforts to preserve mussels in natural streams.

The main goal of the present study is to understand how increasing bed roughness modifies flow, turbulent kinetic energy and the dynamics of vortical structures around an isolated, partially-burrowed mussel shell (Figure 1). A related goal is to quantify the effect of increasing bed roughness on the mean drag forces acting on the exposed part of the shell and the associated drag coefficients, and on mixing between the excurrent siphon jet and the surrounding flow. To fully understand the effect of increasing the bed roughness, the study considers cases with different heights, h, of the exposed part of the mussel, as the interactions between the eddies generated by the rough bed and the exposed part of the shell are controlled to a large degree by the d_{50}/h ratio. In the limiting case where d_{50}/h approaches one, the emerged part of the mussel will behave as a bed particle and the flow around the mussel will not differ much from the flow around other particles present on the bed surface. The study of H. Wu, Constantinescu, and Zeng (2020) has shown that increasing the filtering ratio *VR* between the excurrent velocity, U_{ex}, and the section-averaged or bulk channel velocity, U_o, increases the drag force acting on the shell which suggests that mussel should limit their filtering activity at high flow conditions to better resist dislocation from the substrate. The present study will investigate if this is also the case for a different species of freshwater mussel

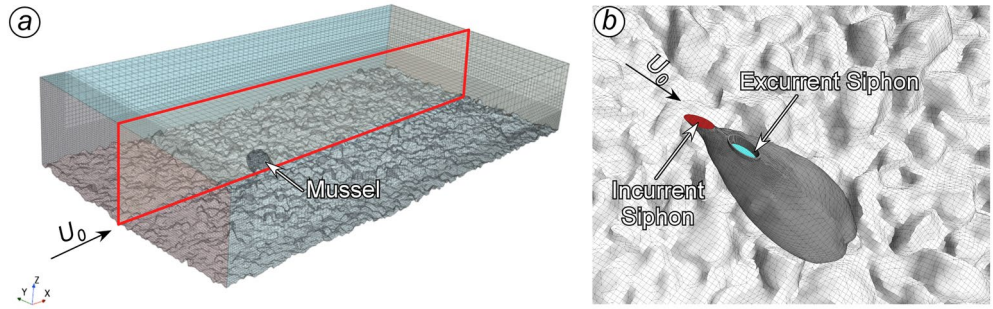

Figure 2. Computational domain and rough bed surface. (a) three-dimensional (3-D) view of the computational domain (red rectangle shows the $y/H = 0$ plane); (b) 3-D view of the mussel, highlighting the positions of the incurrent and excurrent siphons.

whose geometry is quite different from the one considered by H. Wu, Constantinescu, and Zeng (2020) and if the drag force variation with increasing *VR* follows a similar trend once the bed becomes rough.

Other research questions the present study tries to answer are: (a) how does bed roughness affect the formation and strength of the base vortices induced by active filtering and, possibly, of tip vortices, if present? (b) how is wake vortex shedding affected by increasing bed roughness in terms of the capacity of the flow to generate billow vortices and the dominant mechanism that leads to the formation of these vortices? and (c) do filter feeding effects on the near-bed flow increase or decrease with increasing bed roughness? The present investigation provides information for a limiting canonical case (isolated mussel on a rough bed) with respect to which the physics of more complex cases (e.g., clusters of mussels and large arrays of mussels placed on a rough bed) can be investigated in a systematic way.

The paper is organized as follows. Section 2 presents the test cases used to numerically investigate the effects of varying the bed roughness, d_{50}, filtering velocity ratio, *VR*, and height of the exposed part of the mussel, *h*, on flow, turbulence structure, drag forces and dilution of the excurrent jet flow. Section 2 also describes the numerical model, the boundary conditions and the grids used in the simulations, and reports results of a validation simulation using new velocity data collected from a laboratory experiment as part of the present study. Section 3 discusses how the mean flow and turbulent kinetic energy change with varying d_{50}, *h*, and *VR*. Section 4 focuses on the vortical structures generated in the flow and, in particular, the dynamics of the base and tip vortices. Section 5 analyzes the structure of the near-wake flow including the formation of regions of strong downwelling and upwelling motions and the wake vortex shedding modes. The influence of d_{50}, *h*, and *VR* on the horizontal drag forces and associated streamwise drag coefficient is discussed in Section 6. Section 7 uses a passive scalar introduced through the excurrent siphon to quantify dilution of the excurrent siphon jet. The main findings are summarized in Section 8 that also provides some final discussion and conclusions.

2. Test Cases, Computational Approach and Model Validation

2.1. Test Cases

The simulations discussed in the present study were performed in a nearly rectangular channel, 0.360 m wide and 0.690 m long (Figure 2a). The bed surface used in the rough-bed simulations was based on a reproduction of a water-worked gravel bed sample from laboratory, with $d_{50} = 3.10$ mm and $d_{90} = 5.00$ mm (Section 2.5). In present study the main focus was on the flow around the partially-buried mussel. As such, the critical effect related to the presence of a gravel bed that the simulations needed to capture was the generation of turbulent eddies by the exposed part of the roughness elements and their interaction with the emerged part of the mussel. For this reason, the bed was assumed to be impermeable; only the part of the gravel bed directly exposed to the overflow was modeled without considering the lower part of the gravels and the pores below them. Additional simulations were performed with a flat bed (i.e., $d_{50} = 0.00$ mm) and with a deformed bed surface of lower roughness, obtained by multiplying the vertical elevation of the original gravel bed by a factor 0.5. For this new surface of lower roughness, $d_{50} = 2.46$ mm.

The flow depth in the smooth-bed simulations was $D = 0.103$ m, the same as the average flow depth in the corresponding rough-bed simulations (within the rigid-lid approximation, see Section 2.3, this corresponds to change

the energy slope). The flow rate through the channel was $Q = 0.0061$ m³/s, corresponding to a section-averaged, or bulk, velocity $U_0 = 0.164$ m/s.

The geometry of the emerged part of the mussel shell (Figure 1) was obtained from a real shell of an *Unio elongatulus* mussel, which is a popular freshwater mussel in riverine and lake environments in Northern Italy (Froufe et al., 2017; Lopes-Lima et al., 2017; Marrone et al., 2019). The mussel specimen had a shell that is 0.08 m long. Based on field observations, the mussel was placed with its major axis forming a 45° angle with the bed, according to its usual position in the real habitat, as pictured in Figure 1. The mussel was aligned parallel to the incoming flow (i.e., the angle of attack is 0°). In this configuration, the projected mussel length along the streamwise direction was $L = 0.055$ m, the projected total height along the vertical direction was $H = 0.050$ m and the maximum width of the mussel was $b = 0.020$ m. Considering the exposed part of the mussel, while the length, L, and the width, b, remained approximatively the same for the different levels of mussel burial considered in the present study, the height of the mussel above the bed surface, h, decayed with increasing mussel burrowing. The incurrent siphon was pointing upstream, while the excurrent siphon, which was located downstream of the incurrent siphon, was pointing upwards (Figure 2b). The small change in the volume of the shell associated with the opening of the shell during the filtering process was neglected. The flux rates through the incurrent and excurrent siphons were equal ($Q_{in} = Q_{ex}$), and the values used in the simulations were 0.0, 1.55×10^{-6} and 3.10×10^{-6} m³/s. Since the exhaling siphon cross section was 1.1 time larger than that of the inhaling siphon, lower values of velocity were prescribed at its boundary to maintain the discharges through the two siphons equal to each other. The excurrent siphon velocities, U_{ex}, were 0.0, 0.1, and 0.2 m/s, respectively. The corresponding values of the velocity ratio, $VR = U_{ex}/U_0$, were 0, 0.61, and 1.22. The highest value ($VR = 1.22$) is close to the upper threshold observed for mussels of this size (Bunt et al., 1993). The intermediate value ($VR = 0.61$) corresponds to the average filtering discharge for several mussels of similar size (Monismith et al., 1990; Sansom et al., 2018).

Simulations with $VR = 0$ were performed considering three different levels of mussel burial ($h = 0.024$, 0.019, and 0.014 m corresponding to $h/H = 0.48$, 0.38, and 0.28, respectively) for the case when the mussel was placed on the rough bed with $d_{50} = 3.10$ mm described above ($d_{50}/H = 0.062$). Two more simulations with $VR = 0$ and $h/H = 0.48$ were performed with a reduced bed roughness ($d_{50}/H = 0.049$) and with a smooth bed ($d_{50}/H = 0$). To investigate the effect of the active filtering, these previous five simulations were repeated using $VR = 0.61$ and $VR = 1.22$. The main flow and geometrical parameters of the 15 simulations are summarized in Table 1.

Since typically mussels are not encountered in very shallow water, the numerical simulations described in Table 1 considered a relatively high submergence (i.e., $D/h > 4$). This ratio was shown to be an important parameter in studies of flow around symmetrical, submerged objects (e.g., Hajimirzaie et al., 2012; Papanicolaou et al., 2018; Singh et al., 2019). Cases with $D/h > 4$ correspond to the regime 1 identified by Shamloo et al. (2001), in which the interactions between the water surface and the wake are negligible. Much shallower cases (e.g., $D/h < 1.5$) with strong obstacle-free surface interactions are characterized by different, more complex flow physics (Lacey & Rennie, 2012; Sadeque et al., 2008, 2009). Such cases are less relevant for mussels in natural streams. One should also mention that additional simulations were performed with a lower flow depth ($D = 0.069$ m, $D/h = 2.9$) for $h/H = 0.48$, $d_{50}/H = 0.062$ and three different values of VR (i.e., 0.00, 0.61, and 1.22). We noticed negligible differences between the corresponding simulations performed with $D = 0.069$ m and $D = 0.103$ m. Given that the results of the simulations conducted with different values of the submergence ratio were very close to each other, the simulations conducted with $D = 0.069$ m are not included in Table 1.

2.2. Numerical Model

The simulations were performed using the finite-volume, viscous flow solver in STAR-CCM+. Detached Eddy Simulation (DES) was used to resolve the dynamics of the energetically important eddies in the flow. DES is a hybrid approach that reduces to Reynolds-Averaged-Navier-Stokes (RANS) equations near the solid boundaries (Heinz, 2020; Menter et al., 2021). The Large Eddy Simulation (LES) mode is active over the rest of the computational domain (K. Chang et al., 2007a). The base RANS model in the present simulations was the Shear Stress Transport (SST) k-ω model (Menter, 1994; Menter et al., 2003). The turbulence length scale in DES is redefined such that it becomes proportional to the local grid size away from the solid boundaries and the eddy viscosity becomes proportional to the square of the local grid spacing, like in classical LES. In the present simulations, a scalar transport equation was solved for the passive scalar introduced in the excurrent siphon (Figure 1). The scalar was used to study the dilution of the excurrent-jet siphon with a unity Prandtl number, which is generally

Table 1
Matrix of Test Cases With Relevant Flow and Geometrical Properties

h/H (–)	d_{50}/H (–)	$VR = U_{ex}/U_0$ (–)	L/H (–)	b/H (–)	b/L (–)	h/b (–)	d_{50}/h (–)	L_R/h (–)	A_x/H^2 (–)	$F_{dx}/\rho U_0^2 H^2$ (–)	$F_{dy}/\rho U_0^2 H^2$ (–)	$F_{dxy}/\rho U_0^2 H^2$ (–)	C_{dx}^{MEAN} (–)	C_{dx}^{RMS} (–)
0.48	0.062	0	1.02	0.40	0.39	1.20	0.13	2.3	0.131	0.0105	0.0016	0.0106	0.160	0.013
0.38	0.062	0	0.98	0.40	0.41	0.95	0.16	2.6	0.096	0.0057	0.0004	0.0057	0.119	0.019
0.28	0.062	0	0.94	0.40	0.43	0.70	0.22	3.2	0.050	0.0024	0.0003	0.0025	0.097	0.019
0.48	0.049	0	1.00	0.40	0.40	1.20	0.10	2.3	0.131	0.0102	0.0012	0.0103	0.155	0.007
0.48	0.000	0	0.96	0.40	0.42	1.20	0.00	2.7	0.131	0.0099	0.0007	0.0100	0.152	0.007
0.48	0.062	0.61	1.02	0.40	0.39	1.20	0.13	2.4	0.131	0.0113	0.0026	0.0116	0.172	0.015
0.38	0.062	0.61	0.98	0.40	0.41	0.95	0.16	2.6	0.096	0.0064	0.0024	0.0069	0.135	0.026
0.28	0.062	0.61	0.94	0.40	0.43	0.70	0.22	3.2	0.050	0.0028	0.0012	0.0031	0.113	0.023
0.48	0.049	0.61	1.00	0.40	0.40	1.20	0.10	2.4	0.131	0.0111	0.0015	0.0112	0.169	0.007
0.48	0.000	0.61	0.96	0.40	0.42	1.20	0.00	2.9	0.131	0.0107	0.0008	0.0107	0.163	0.009
0.48	0.062	1.22	1.02	0.40	0.39	1.20	0.13	2.5	0.131	0.0094	0.0027	0.0098	0.143	0.016
0.38	0.062	1.22	0.98	0.40	0.41	0.95	0.16	2.9	0.096	0.0043	0.0017	0.0047	0.091	0.010
0.28	0.062	1.22	0.94	0.40	0.43	0.70	0.22	3.6	0.050	0.0015	0.0008	0.0017	0.060	0.022
0.48	0.049	1.22	1.00	0.40	0.40	1.20	0.10	2.7	0.131	0.0092	0.0021	0.0095	0.141	0.007
0.48	0.000	1.22	0.96	0.40	0.42	1.20	0.00	3.1	0.131	0.0086	0.0012	0.0087	0.132	0.007

Note. Variables h, H, L, b, U_{ex}, U_0 are defined in Figure 1; d_{50} is the mean grain size of the rough bed; L_R is the length of the recirculation region at the back of the mussel; $A_x(h)$ is the projected frontal area in the x-direction; F_{dx}, F_{dy}, and F_{dxy} are the streamwise, spanwise and total horizontal drag forces acting on the exposed part of the mussel shell; C_{dx}^{MEAN} and C_{dx}^{RMS} are the mean streamwise drag coefficient and the root mean square of the streamwise drag coefficient, respectively.

assumed for this type of investigations (K. Chang et al., 2007b). All governing equations were integrated through the viscous sublayer to avoid the use of wall functions. DES calculations that resolve the viscous sublayer were shown to accurately predict flow and turbulence statistics for complex turbulent flows such as flow in natural channels and flow past surface-mounted obstacles (Constantinescu, 2014; Constantinescu & Squires, 2003; Constantinescu et al., 2003; Keylock et al., 2012; Kirkil & Constantinescu, 2009).

The governing equations were discretized on unstructured, nested, Cartesian-like grids. The Navier-Stokes equations were advanced in time using a Semi-Implicit Method for Pressure Linked Equations (SIMPLE) algorithm in which an intermediate velocity is calculated by solving the momentum equations without the pressure term and then the final velocity is obtained using a pressure correction that ensures the continuity equation is satisfied (Patankar & Spalding, 1972; Qin et al., 2021; Xu et al., 2022). The convection terms in the momentum equations were discretized using a Hybrid-Bounded central difference scheme, which couples a higher-order upwind scheme in regions where the RANS mode is active with a bounded central difference scheme in regions where the LES mode is active. The second-order upwind scheme was used to discretize the convective terms in the transport equation for the eddy viscosity and the passive scalar, while the second-order central scheme was used for the diffusive and pressure gradient terms. The temporal discretization was implicit. The solver was parallelized using message passing interface. DES simulations performed using the STAR-CCM+ solver were shown to accurately predict complex flows containing highly-unsteady vortices, and steady and unsteady flows in channels containing large-scale flow obstructions (Horna-Munoz & Constantinescu, 2018; Lazzarin et al., 2023; P. Wu, Horna-Munoz, et al., 2020).

2.3. Computational Model and Boundary Conditions

The gravel bed surface and the geometry of the mussel shell were reproduced from real samples. They were reconstructed separately with an accurate close-range photogrammetric survey (ground sample distance of ~0.06 mm), a technique that was shown to well capture the geometry of gravel beds (Chen et al., 2019). We used a Nikon D5200 digital camera and a classical Structure from Motion and Multi-View Stereo matching approach for image orientation and dense point cloud production (Carrivick et al., 2016). The image processing was performed with the Agisoft Metashape software. The point clouds, consisting of 1.9 million points for the 0.4 m wide and 1.0 m

long bed surface, and of 172,000 points for the mussel shell, were exported as a triangulated meshes in stereolithography files (*.stl*), with a spatial resolution up to 0.4 mm for the bed and 0.1 mm for the mussel shell. These files were subsequently imported into the grid generator of STAR-CCM+ where the mussel was cut corresponding to the desired level of burial and placed on a smooth or a rough bed (Figure 2a). No-slip boundary conditions were then applied on the surfaces of the deformed bed and the emerged part of the mussel. The turbulent kinetic energy was set equal to zero on all solid surfaces. The standard relationships were used to specify the turbulence vorticity on these surfaces (Menter, 1994).

To mimic the incurrent and the excurrent siphons (Figure 2b), two additional parts were added to the mussel-shell geometry. To capture more realistically the interaction between the excurrent siphon jet and the overflow, a vertical pipe connecting to this siphon was added inside the upper part of the mussel, as in H. Wu, Constantinescu, and Zeng (2020). A fixed mass flow corresponding to the desired filtering flow discharge was specified on the incurrent siphon surface and at the inlet section of the excurrent siphon pipe. A concentration $C_0 = 1$ was imposed at the inlet section of the pipe. For simulations conducted with no active filtering, the excurrent pipe was removed and a cap was placed on the top of the excurrent siphon.

The rigid-lid approximation was used to specify the boundary conditions (e.g., zero shear stress for velocity, zero vertical gradient for the other variables) at the upper boundary of the computational domain. This approximation is acceptable given the low channel Froude number ($F = 0.16$) in the corresponding experiments and the high submergence of the emerged part of the shell (Hajimirzaie et al., 2012; Koken & Constantinescu, 2009; H. Wu, Constantinescu, & Zeng, 2020). A symmetry boundary condition was imposed at the two lateral boundaries, while a pressure outlet boundary condition was imposed at the exit section. At the channel inlet section, the mean velocity was obtained from a preliminary simulation conducted in a channel with the same cross section at the inlet section and of length 0.36 m. Periodic boundary conditions were imposed in the streamwise direction in the preliminary simulation to obtain a fully-developed velocity profile. The passive scalar concentration, C, was set to 0 at the channel inlet boundary. At the channel exit boundary, C was set to be equal to the value at the immediate interior cell. On the other surfaces, the gradient of C in the direction normal to the surface was set to zero. More details on the boundary conditions are given in H. Wu, Constantinescu, and Zeng (2020) who used a similar approach to conduct simulations past a mussel placed on a smooth bed. The precursor simulation also provided the inlet distributions of the turbulent kinetic energy, k, and the turbulence vorticity, ω, for which transport equations are solved in the present SST-based DES model. These variables were extrapolated from the interior of the domain on the top, lateral and exit surfaces.

2.4. Computational Mesh

Similar to H. Wu and Constantinescu (2022), the computational mesh was generated using the grid generator in STAR-CCM+. The computational domain was meshed using mostly of hexahedral cells. In the immediate vicinity of irregular surfaces, the grid generator uses automatic mesh refinement and trimmed cells to provide a conformal mapping of the deformed surface. This procedure also results in smooth transitions between regions of lower and higher levels of mesh refinement. Regions close to the mussel and to the deformed bed surface required high levels of mesh refinement to represent the surface with a sufficient degree of precision and to resolve the attached boundary layers.

The computational domain was decomposed into three main regions with a progressive decrease in the dimensions of the computational cells as the bed and the mussel are approached. In the upper region, the average size of the computational cells was close to 0.0048 m. The average size of the cells near the bed and the shell was close to 0.0012 m. Close to the mussel's shell, the average cell size in the direction tangent to the shell surface was about 20–25 wall units. At least one grid point was situated inside the viscous sublayer in the wall normal direction. The regions surrounding the siphons were meshed with an even higher resolution (0.0005 m). Using the aforementioned rules, the meshes used in the rough-bed simulations contained close 6 million cells.

The numerical predictions were shown to be grid independent. We performed several simulations for the rough-bed case with different levels of grid refinement and checked the sensitivity in terms of the predicted values of velocity, vorticity (x, y, z components) and TKE. The grid sizes in the near bed region ranged between 0.0008 and 0.0030 m in the simulations performed to check the grid independency of the solution. The mesh size in the part of the domain situated in the vicinity of the deformed bed surface was 0.0012 m for the numerical simulations

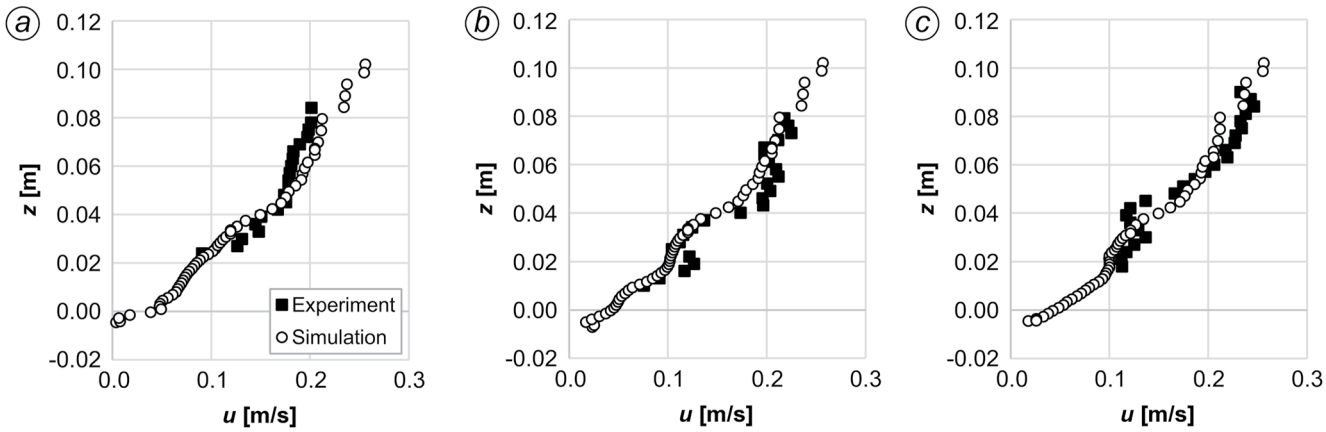

Figure 3. Vertical profiles of mean streamwise velocity at points *P*1 (a), *P*2 (b), and *P*3 (c) (see Figure 1) predicted by the validation simulation and measured experimentally over a rough bed ($d_{50}/H = 0.062$).

reported in Table 1. Simulations conducted with higher resolution near the bed surface showed negligible variations of the above variables with respect to results obtained with a resolution of 0.0012 m near the bed.

The same code was already used to conduct simulations of flow past mussels and grid sensitivity studies were conducted by H. Wu, Constantinescu, and Zeng (2020) to determine the minimum grid resolution around the mussel needed to obtain accurate and grin-independent results. The Reynolds numbers and the level of mesh refinement in the region around the mussel were similar to those of the present study. Due to the presence of the irregular gravel bed and the need to resolve the turbulence generated by the roughness elements, for the number of computational cells used in the simulations reported in the present study is roughly three times higher than for the number of grid cells used by H. Wu, Constantinescu, and Zeng (2020) and H. Wu and Constantinescu (2022) to simulate flow past a partially-burrowed mussel placed on a smooth, flat bed.

2.5. Model Validation

Though the numerical model was already validated for flow past isolated, partially-burrowed mussels by H. Wu, Constantinescu, and Zeng (2020), the present study provides additional validation of the model for the case the mussel is placed on a rough bed corresponding to a gravel bed with $d_{50} = 3.10$ mm.

A laboratory experiment of flow around a mussel, placed on the gravel bed previously described, was performed in a recirculating flume 11 m long and 0.40 m wide at the Hydraulic Laboratory of the Department of Engineering—University of Palermo. Nearly uniform flow conditions with water depth $D = 0.103$ m was achieved by setting a gate at the downstream section of the flume. The height of the exposed part of the mussel was $h = 0.024$ m, corresponding to a submergence ratio $D/h = 4.3$, with no active filtering by the mussel. The flow rate per unit width was the same as in the numerical simulations. The streamwise velocity was measured with a vertical resolution of 0.003 m at the inlet and along three verticals around the mussel, as shown in Figure 1, using a non-intrusive ultrasonic velocity profiler DOP2000 by Signal Processing S.A. (probes with emission frequency of 2 MHz, pulse repetition frequency in the range 4,000–5,000 Hz, accuracy of 0.0009 m/s).

The flow conditions, bed surface, and width of the computational domain in the validation simulation were based on the experimental data, and the mesh density was the same as for the simulations listed in Table 1. In this simulation, the lateral boundaries were treated as smooth walls to mimic the experimental conditions. At the inlet, the vertical streamwise velocity profile obtained from experimental measurements conducted in the symmetry plane of the flume was assumed to be constant along the width of the section. The rest of the boundary conditions were identical to the ones discussed in Section 2.2.

Figure 3 compares the numerical prediction of the mean streamwise velocity at several horizontal locations (P1, P2, and P3) shown in Figure 1. The level of agreement is overall very satisfactory taken into account that only one vertical profile was measured at the inlet section, which means that the effects of secondary flow and lateral nonuniformity of the streamwise velocity field in the incoming flow (e.g., due to the irregular distributions of the

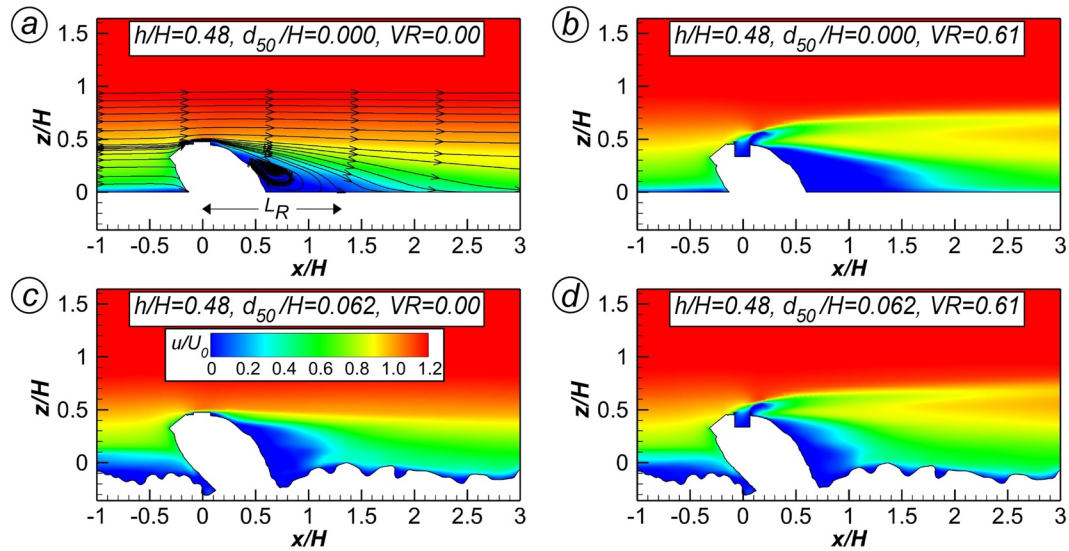

Figure 4. Mean streamwise velocity, u/U_0, in the $y/H = 0$ plane for different simulations (a–d). L_R denotes the maximum streamwise length of the mean-flow recirculation region based on 2-D streamline patterns.

rough-bed particles) were ignored. Moreover, the level of agreement between the measured and predicted vertical profiles of the streamwise velocity is similar to that observed by H. Wu, Constantinescu, and Zeng (2020) for the case of a semi-burrowed mussel placed on the smooth, horizontal bed of an open channel.

3. Mean Flow and Turbulent Kinetic Energy

Similar to other types of flow past submerged surface-mounted obstacles, a recirculation region forms at the back of the mussel. The flow moving over the top of the mussel plunges back toward the bed. The maximum streamwise distance, measured from the position of the point of highest elevation of the mussel shell, to the point at which the flow reattaches in the near wake is denoted L_R (see Figure 4a where the recirculation bubble is visualized using mean 2-D streamlines in the $y/H = 0$ vertical plane for the $h/H = 0.48$, $d_{50}/H = 0$, $VR = 0$ case). The presence of sediment particles induces the formation of a near-bed region of reduced streamwise velocities upstream of the mussel's shell in the rough bed simulations (Figures 4c and 4d) which should affect the adverse pressure gradients generated in front of the mussel and the eventual formation of horseshoe vortices. By contrast, the thickness of this region is fairly negligible in the near wake. The active filtering also modifies the streamwise velocity distribution behind the mussel independently of the bed roughness value. The increase in the height of the region of reduced streamwise velocities with increasing VR (e.g., compare cases with $VR = 0$ in Figures 4a and 4c and $VR = 0.61$ in Figures 4b and 4d) is driven by the excurrent siphon jet that changes direction from vertical to horizontal in the near wake. These changes are important as they affect the transport of nutrients and organic matter around the mussel.

Though a recirculating flow region is present in all the simulations, the size of the bubble, as measured by its streamwise length L_R, changes as a function of the bed roughness and filtering discharge (Figure 4). Given that the size of the recirculation region behind a surface-mounted obstruction scales with the height of the obstruction, Figure 5 shows the variation of L_R/h. The most important effect is the decrease of L_R/h with increasing bed roughness (Figure 5a), which is mainly driven by the amplification of the turbulence dissipation in the near wake, as the wake flow interacts with the sediment particles at the bed surface. This effect is observed for cases with and without active filtering. For $VR < 1$, the decrease of L_R/h in the $h/H = 0.48$ rough-bed simulations is of the order of 25% compared to the corresponding smooth-bed simulation. Results in Figure 5a also show that for constant bed roughness, L_R/h increases monotonically with VR, with a rate that is decreasing with increasing bed roughness. The other important effect is the decrease of L_R/h with decreasing level of mussel burial. The rates of decrease of L_R/h with h/H for the rough bed cases with $d_{50}/H = 0.062$ in Figure 5b are fairly independent of the value of VR. A similar trend in the variation of L_R/h with h/H was predicted by H. Wu, Constantinescu, and Zeng (2020) for an isolated mussel (*L. siliquidea*) placed on a smooth bed.

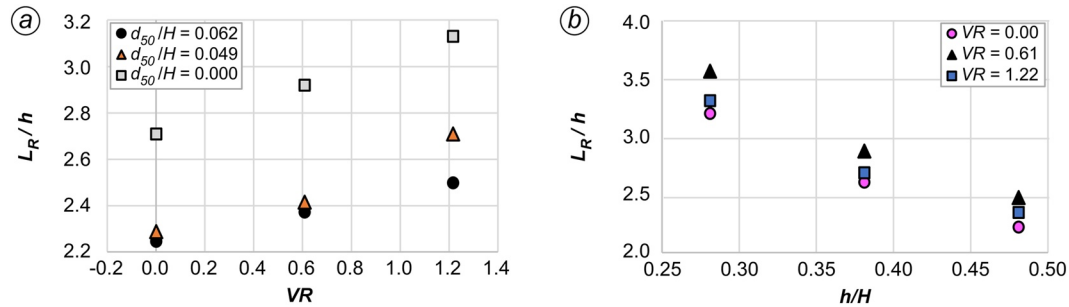

Figure 5. Nondimensional length of the recirculation region, L_R/h, (see Figure 4a) for different values of the bed roughness, d_{50}/H, as a function of the velocity ratio VR in the $h/H = 0.48$ simulations (a), and for different values of VR, as a function of the mussel burrowing level in the $d_{50}/H = 0.062$ simulations (b).

As opposed to the mussel considered in the study of H. Wu, Constantinescu, and Zeng (2020), no mean-flow horseshoe vortices form around the upstream face of the mussel in the smooth-bed simulations (Figures 6a and 6b). This is a consequence of the vertical tilt of the major axis of the mussel and of the more streamlined shape of the mussel. Thus, depending on the shape of the mussel and how the mussel is anchored in the substrate, one important mechanism for local bed erosion around the mussel (i.e., local scour driven by horseshoe vortices) may be absent.

Though in the rough-bed cases the main vorticity sheet in the flow approaching the mussel is situated above the top of the largest bed particles near the mussel, no large vortices form near the junction line between the mussel and the bed surface (Figures 6c and 6d). Increasing the bed roughness in the simulations with no active filtering reduces the length of the separated shear layer forming at the top of the mussel, a result consistent with the decrease of L_R with increasing d_{50}/H in Figure 4. In this case, the tilt with respect to the horizontal direction is also reduced. In the simulations with $VR > 0$, a second shear layer forms in between the outer flow moving over the mussel and the excurrent siphon jet.

Consistent with the mean vorticity distributions in Figure 6, that show no evidence of the presence of horseshoe vortices for the smooth bed cases, the corresponding *TKE* distributions in Figures 7a–7c show no amplification of the turbulence at the base of the mussel compared to the levels in the incoming fully-developed turbulent flow. Some amplification of the *TKE* is observed at the base of the mussel in the rough bed cases especially for relatively large values of the filtering discharge (Figures 7f and 7i) though it is not clear if this amplification is related to the generation of horseshoe vortices in the instantaneous flow fields or simply to larger-scale turbulence in between the bed surface and the main sheet of vorticity forming upstream of the mussel (Figure 6).

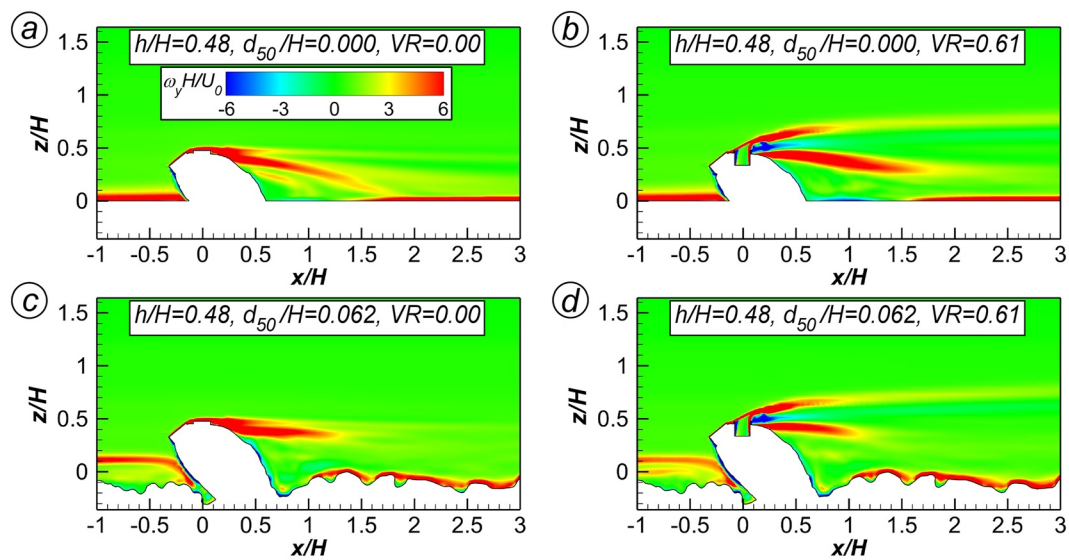

Figure 6. Mean flow spanwise vorticity, $\omega_y H/U_0$, in the $y/H = 0$ plane for different simulations (a–d).

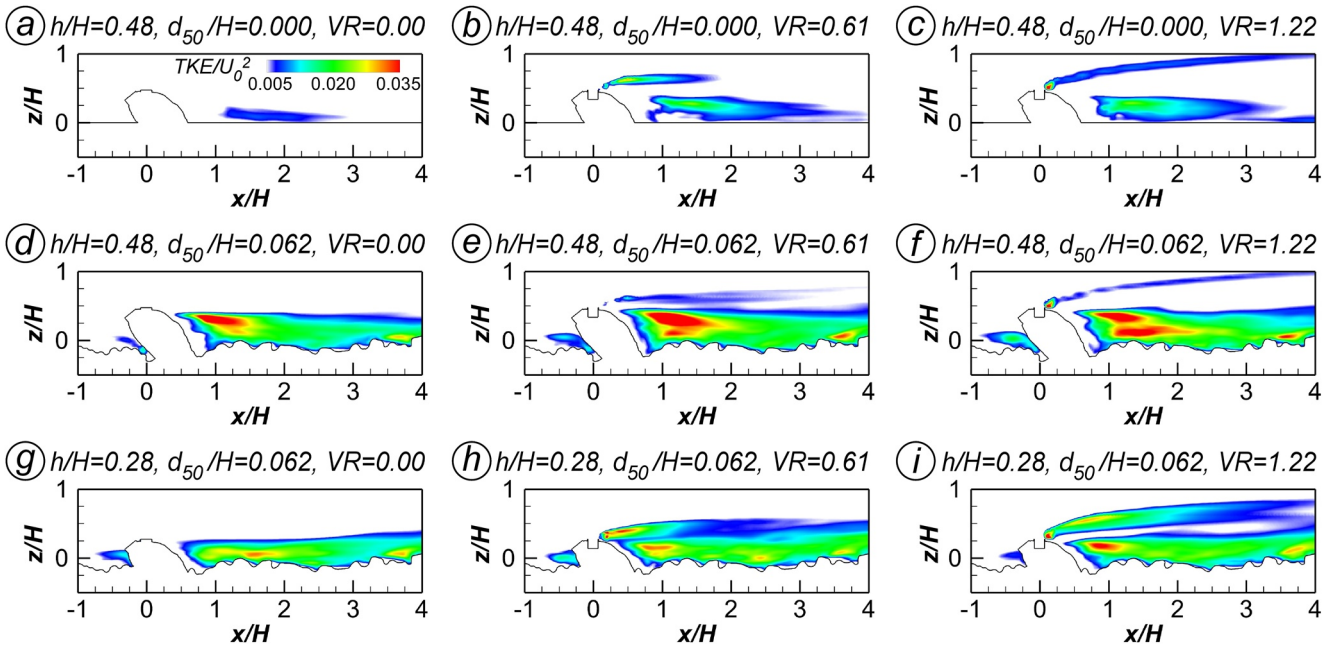

Figure 7. Turbulent kinetic energy, TKE/U_0^2, in the $y/H = 0$ plane for different simulations (a–i). Values lower than 0.007 were blanked.

The *TKE* levels are relatively low inside the near-wake region in the smooth bed case with no active filtering (Figure 7a). The peak values are close to one order of magnitude lower than those observed by H. Wu, Constantinescu, and Zeng (2020) in their corresponding simulations. The main reason is that for the present mussel shape and mussel orientation with respect to the bed, the anti-symmetric vortex shedding, which is the main mechanism for the amplification of the *TKE* behind the mussel, is basically suppressed in the absence of siphonal activity (see discussion in Section 5). The presence of moderate or strong active filtering allows the formation of wake vortices via anti-symmetric shedding in the smooth bed cases (Figures 7b and 7c). Still, the *TKE* levels in these cases remain about 50% lower than those observed by H. Wu, Constantinescu, and Zeng (2020) for similar values of h/H and *VR*. Increasing the bed roughness induces a strong amplification of the antisymmetric vortex shedding mode in the wake (Figure 7d–7i), which explains the larger values of the *TKE* in the rough bed simulations compared to the corresponding smooth bed simulations. For $h/H = 0.48$, the *TKE* values inside the near wake are close to 100% larger for $d_{50}/H = 0.062$ compared to the smooth-bed predictions (e.g., compare cases in Figures 7a–7c and Figures 7d–7f). A secondary region of high *TKE* is generated on the inner part of the excurrent-siphon jet in the simulations with $VR \geq 0.61$ (Figures 7e, 7f, 7h, and 7i). For constant bed roughness, the *TKE* in the near wake increases with decreasing the burial level of the mussel (e.g., compare cases in Figures 7d–7f and Figures 7g–7i). This is somewhat expected, given that if h becomes close to d_{50}, the emerged part of the shell will behave like a large bed particle.

4. Main Vortical Structures Generated Around the Mussel

The Q criterion is used in Figure 8 to visualize the large-scale coherent structures in the instantaneous and mean flow fields for some representative test cases. Consistent with the vorticity and *TKE* distributions in the $y/H = 0$ plane (Figures 6 and 7), the vortical structures visualized in Figure 8 and the 2-D mean streamline patterns in Figure 9 offer further confirmation that no horseshoe vortices are forming around the upstream base of the mussel in the simulations conducted with a smooth bed. This is the true regardless of the value of *VR* (e.g., see results for smooth-bed simulations in Figure 8). For similar cases, H. Wu, Constantinescu, and Zeng (2020) observed the formation of horseshoe vortices in the mean and instantaneous flow fields. The difference can be attributed to the lower degree of bluntness of the mussel used in the present study. Still, one expects that some weak vortices will form even for more streamlined mussel shells. The main reason is likely the different inclination of the mussel (e.g., the tilt of the top of the mussel toward the incoming flow), which results in a much weaker downflow parallel to the front face of the mussel. The formation and coherence of the horseshoe vortices scale with the strength of the downflow (Kirkil & Constantinescu, 2009; McCoy et al., 2007).

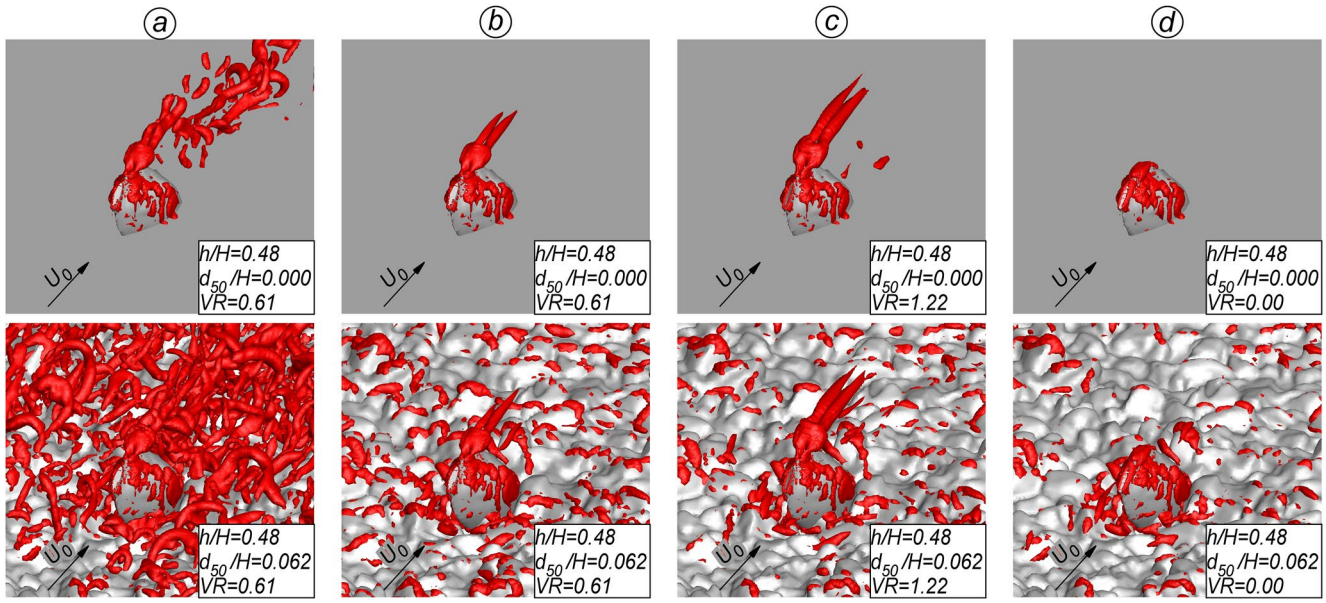

Figure 8. Coherent structures visualized using the Q criterion. (a) instantaneous flow, $h/H = 0.48$, $VR = 0.61$ simulations with $d_{50}/H = 0$ and 0.062; (b) mean flow, $h/H = 0.48$, $VR = 0.61$ simulations with $d_{50}/H = 0$ and 0.062; (c) mean flow, $h/H = 0.48$, $VR = 1.22$ simulations with $d_{50}/H = 0$ and 0.062; (d) mean flow, $h/H = 0.48$, $VR = 0.00$ simulations with $d_{50}/H = 0$ and 0.062.

Even in the rough-bed simulations, no well-defined horseshoe vortices are present in the mean and instantaneous flow fields (Figure 8). Though 2-D streamline patterns in vertical sections cutting through the mussel seem to suggest the presence of horseshoe vortices in the rough bed cases (Figure 9a), the Q criterion visualizations in Figure 8 show that the eddies present near the junction line between the bed and the shell do not extend around the upstream base of the shell. Rather, they are just eddies generated by flow separation in between the larger particles present at the bed. Though the formation of these eddies near the mussel is favored by the adverse pressure gradients induced by the shell, these eddies cannot be considered horseshoe vortices.

The Q criterion visualizations also show the presence of a pair of fairly symmetric vortices originating near the excurrent siphon in all the smooth and rough bed simulations conducted with $VR \geq 0.61$ (Figures 8b and 8c). The coherence of these vortices increases with increasing VR. By contrast, no such vortices form in the simulations with the active filtering turned off (Figure 8d). These vortices are different from the pair of counter-rotating base vortices (e.g., vortices that advect fluid upwards in between their cores) forming near the bed surface in the smooth-bed simulations conducted by H. Wu, Constantinescu, and Zeng (2020). One important observation is that most of those simulations were conducted with low values of the excurrent jet flow velocity relative to the section-averaged flow velocity in the channel ($VR \leq 0.13$). In the simulations conducted with $VR = 0.7$, H. Wu, Constantinescu, and Zeng (2020) observed the formation of a second pair of base vortices at elevations close to that of the excurrent siphon, similar to the vortices present in Figure 8b. Because of the larger asymmetry of the

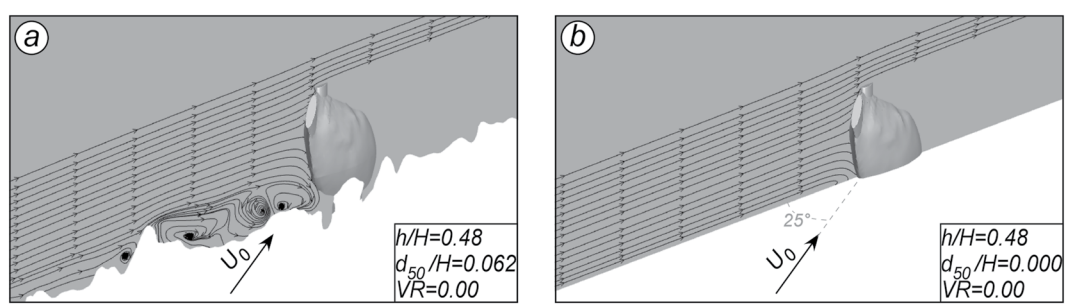

Figure 9. Mean flow, 2-D streamline patterns in a vertical plane making a 25° angle with the $y/H = 0$ plane in the $h/H = 0.48$, $VR = 0.00$ simulations with $d_{50}/H = 0.062$ (a) and $d_{50}/H = 0.000$ (b).

emerged part of the mussel shell, only one of the base vortices was present away from the mussel in the simulations conducted with a relatively large value of h conducted by H. Wu, Constantinescu, and Zeng (2020). Only for a high level of mussel burrowing the coherence of the two base vortices became comparable, similar to the cases investigated in the present study.

Figure 8a offers additional information on the dynamics of these vortices. As opposed to the mean flow, where the two cores are fairly straight and symmetric, a large-scale instability propagates along the cores of the two vortices in the instantaneous flow. The associated waviness allows the cores of the two vortices to get very close to each other at some streamwise locations. These mutual interactions are the main mechanism that leads to the breakup of the cores of the two vortices. As the bed roughness increases, the two cores interact with eddies generated by the larger bed particles. Still, the two vortices are clearly visible in the rough bed simulations conducted with $h/H = 0.48$. One expects the interactions will become even stronger in the cases with a higher degree of mussel burrowing, which should result in a more rapid loss of coherence of these vortices.

Though Figure 8b–8d do not show any evidence of formation of a pair of streamwise-oriented vortices close to the bed surface, such vortices are in fact present in many of the flow fields. These vortices are visualized in Figure 10, that shows the mean streamwise-vorticity and 2-D streamline patterns in the $x/H = 1$ and $x/H = 3$ cross sections. In the smooth-bed cases with no active filtering, these vortices are the main pair of vortices forming in the near wake, as shown in Figure 10a for the $h/D = 0.48$, $d_{50}/H = 0$, $VR = 0$ simulation. The flow is advected toward the bed in between their cores, which means they are tip vortices. Hajimirzaie et al. (2012) observed the formation of similar symmetric, near-bed tip vortices in experiments conducted for flow past semi-ellipsoids mounted on a smooth bed. Similar to the present results, in the experiments the coherence of the two tip vortices remained comparable until the two vortices dissipated completely. The fact that H. Wu, Constantinescu, and Zeng (2020) predicted the formation of near-bed base vortices for $VR = 0$ and $VR = 0.13$ is mostly due to the different shape of the emerged part of the shell.

Once the active filtering becomes important (e.g., $VR = 0.61$), the simulations conducted with a smooth bed show the formation of a pair of near-bed tip vortices and of a pair of base vortices situated slightly above the top of the mussel (Figure 10b). The presence of a coherent pair of base vortices in the vicinity of the bed induces a region of strong flow downwelling in between the cores of the two vortices. Meanwhile, the base vortices play an important role in the mixing between the excurrent jet fluid and the surrounding flow.

Once the bed roughness increases, the degree of symmetry of the tip vortices and their coherence decreases with respect to the corresponding smooth bed case mainly because of the interactions of the two vortices with the irregular bed surface. The cores of the two tip vortices are also lifted by the flow in the rough bed simulations (e.g., compare $x/H = 3$ panels in Figures 10a and 10c for $VR = 0$). This means that their capacity to induce strong downwelling near the symmetry plane decreases. The presence of strong active filtering in the rough bed simulations tends to suppress even more the coherence of the tip vortices. In fact, these vortices are not observed in the $x/H = 3$ section in Figure 10d.

The effects of increasing the bed roughness on the base vortices in the $h/D = 0.48$ simulations are much less important compared to the tip vortices, which is somewhat expected given that the base vortices are not situated in the vicinity of the bed. Near the mussel (e.g., see $x/H = 1$ section in Figures 10b and 10d), the circulation of the base vortices is fairly independent of the bed roughness, as also seen from Figure 11a that compares the streamwise variation of the total circulation magnitude Γ_T of the two base vortices. The circulation magnitude, Γ_T, is calculated by integrating the streamwise vorticity, ω_x, in cross-stream (x = constant). The threshold value used to perform the integration over the cores of the vortices is $|\omega_x H/U_0| = 0.3$. At larger distances, the cores of the two vortices are not anymore symmetric with respect to the $y/H = 0$ plane and their total circulations are quite different (e.g., see $x/H = 3$ section in Figures 10b and 10d). Figure 11a offers a more quantitative estimation of the effect of the bed roughness on the decay of the coherence of the base vortices as measured by their total circulation. For a constant level of mussel burrowing and constant bed roughness, the effect of increasing VR is to increase the coherence and circulation of the base vortices (see also Figure 11b). Given the higher vertical momentum of the excurrent siphon jet, the two vortices will move further away from the bed surface in cases with larger VR. This also means that the effect of the bed roughness will be less felt. This is why the two base vortices remain close to symmetric in the $x/H = 3$ section in the $h/H = 0.48$, $d_{50}/h = 0.062$, $VR = 1.22$ simulation (Figure 10g) while their symmetry is totally lost in the $h/H = 0.48$, $d_{50}/h = 0.062$, $VR = 0.61$ simulation (Figure 10d). Moreover, the rate of decay of the total circulation of the base vortices is larger in the $VR = 0.61$ simulation (Figure 11b).

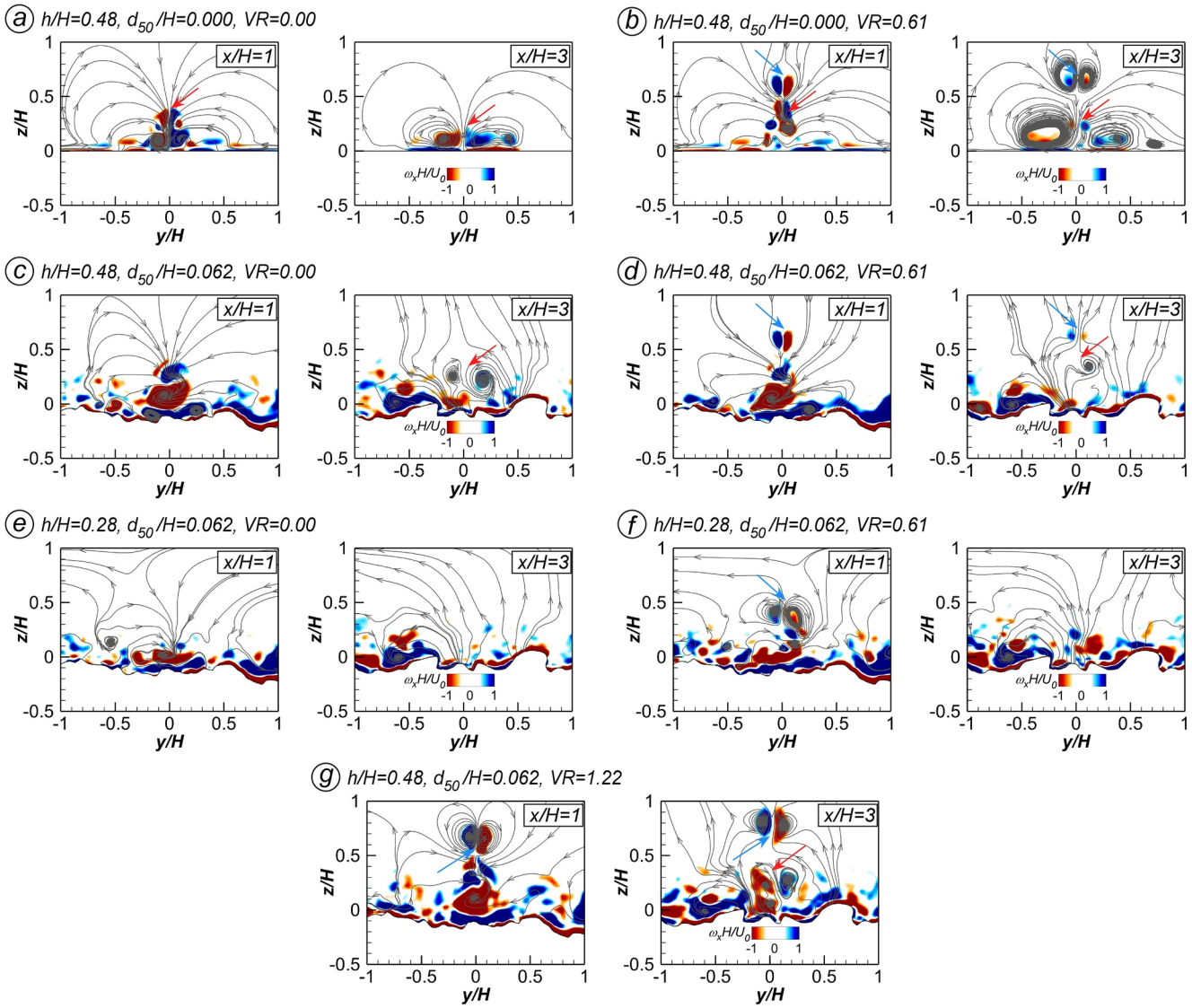

Figure 10. Mean flow streamwise vorticity, $\omega_x H/U_0$ (values between −0.5 and 0.5 were blanked), and 2-D mean streamline patterns in the $x/H = 1$ and $x/H = 3$ planes for different simulations (a–g). The red arrows point toward the tip vortices (downwash flow). The blue arrows point toward the base vortices (upwash flow).

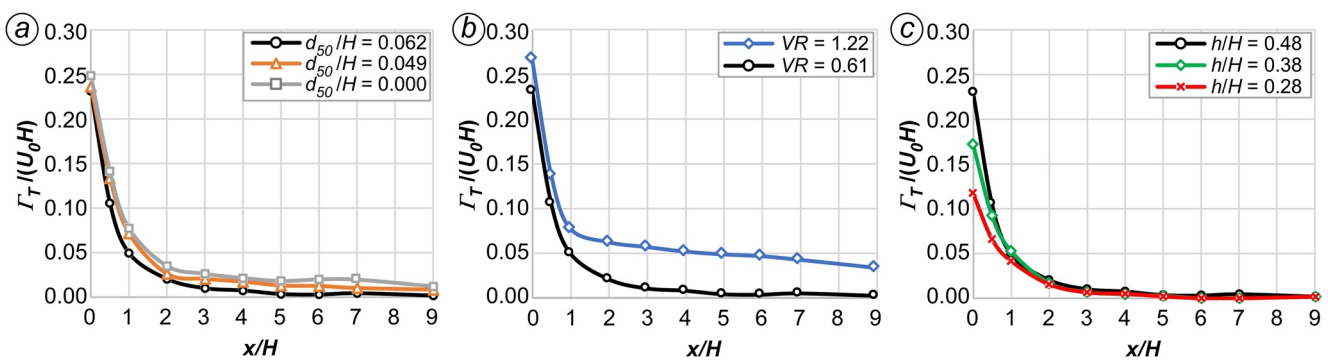

Figure 11. Streamwise variation of the total circulation magnitude of the base vortices, $\Gamma_T/(U_0 H)$. (a) effect of d_{50}/H ($VR = 0.61$, $h/H = 0.48$); effect of VR ($d_{50}/H = 0.062$, $h/H = 0.48$); (c) effect of h/H ($d_{50}/H = 0.062$, $VR = 0.61$).

Finally, it is also relevant to consider the effect of lowering the degree of mussel burial on the dynamics of the base and tip vortices. Only tip vortices form if the active filtering is off. As h decreases, the tip vortices are situated close to the rough bed surface and interact strongly with the largest bed particles. This explains why the tip vortices are destroyed before reaching the $x/H = 3$ section in the $h/H = 0.28$, $d_{50}/H = 0.062$ simulation (Figure 10e, vortices are not present), while they extend way past the $x/H = 3$ plane in the $h/H = 0.48$, $d_{50}/H = 0.062$ simulation (Figure 10c, vortices are present, see the red arrow). The effect of increasing the mussel burrowing for constant bed roughness is even larger in the simulations with a large filtering discharge. For example, tip vortices are absent in the $x/H = 1$ section in the $h/H = 0.28$, $d_{50}/H = 0.062$, $VR = 0.61$ simulation shown in Figure 10f, while tip vortices are still visible in the corresponding simulation with $h/H = 0.48$ (Figure 10d). Moreover, as the degree of burial of the mussel increases, the coherence of the base vortices also decreases (e.g., compare Figure 10d for $h/D = 0.48$ with Figure 10f for $h/D = 0.28$). This effect is illustrated in a more quantitative way in Figure 11c that also shows that the total circulation magnitude of the base vortices decreases monotonically with decreasing h/H starting in their formation region.

5. Near-Wake Flow and Vortex Shedding

The study of H. Wu, Constantinescu, and Zeng (2020) conducted for smooth surfaces found that, for relatively low levels of mussel burial ($h/H \approx 0.5$), the main base vortex generates two large, streamwise-oriented regions of upwelling and downwelling behind the mussel. For higher levels of mussel burrowing ($h/H \approx 0.25$), the coherence of the two base vortices was similar. As a result, a strong region of flow upwelling was generated in between the cores of the two base vortices, near the symmetry axis ($y/H = 0$ plane). This region is bordered by two larger regions of downwelling flow where higher streamwise velocity fluid is advected near the bed. The formation of these regions of flow downwelling was the main reason why larger bed shear stresses were predicted over parts of the near-wake compared to the outer flow.

In the present investigation conducted with a more symmetrical shape of the shell, the circulation of the counter-rotating vortices forming near the bed surface generally remains comparable at large distances from the mussel. Moreover, a pair of tip vortices forms in the smooth bed simulations (Figures 10a and 10b) which induces a region of strong flow downwelling near the symmetry axis ($y/H = 0$) in the $h/H = 0.48$, $d_{50}/H = 0$, $VR = 0$ simulation (Figure 12a). The regions of flow upwelling are close to symmetric, of relatively small size and situated close to the back of the shell. As the downflow reaches the bed surface, it moves away from the symmetry line toward the separated shear layers on the two sides of the mussel. The effect of the active filtering is to reduce the vertical velocity magnitude inside the aforementioned main regions of flow downwelling and upwelling (e.g., see results for the $h/H = 0.48$, $d_{50}/H = 0$, $VR = 0.61$ simulation in Figure 12b), which should also weaken the secondary flow moving from the symmetry plane toward the two separated shear layers.

Further proof that the region of very strong downwelling flow forming in the smooth bed case with no active filtering affects the wake structure in the mean flow is offered by Figure 13 that compares the mean streamwise velocity distribution in the $z/H = 0.25$ plane for the simulations without and with active filtering. In the $VR = 0.61$ simulation (Figure 13b), the shape of the recirculating flow region (negative streamwise velocities) is similar to the one typically observed in the wake of symmetrical bluff bodies and contains two vertical vortices that are the legs of the U-shaped vortex forming at the back of submerged, surface-mounted obstacles (W.-Y. Chang et al., 2020). In the $VR = 0$ simulation (Figure 13a), the recirculation region shrinks significantly. The shape of the wake is very unusual, with two elongated regions of low streamwise velocity forming at the back of the two vortices. As will be discussed later, this happens because the anti-symmetric shedding mode is suppressed due to the strong secondary flow generated by the interaction of the downflow with the bed surface. Finally, the downflow near the upstream face of the mussel is negligible in both smooth bed simulations shown in Figure 13, which is consistent with the absence of horseshoe vortices near the junction line (Figure 9).

In the corresponding rough-bed simulations conducted with $h/H = 0.48$ shown in Figures 12c and 12d, a small region of strong upwelling forms at the back of the mussel followed by a region of flow downwelling near the symmetry plane induced by the counter-rotating tip vortices (e.g., see $x/H = 3$ sections in Figures 10c and 10d). Though base vortices are present, they are situated further away from the bed and have a very limited effect on the vertical velocity pattern near the bed. As already discussed, the symmetry of the tip vortices is lost due to the irregular bed surface, which also explains why the main region of flow downwelling breaks into multiple asymmetrical subregions. As for the corresponding smooth bed cases, the active filtering further weakens the

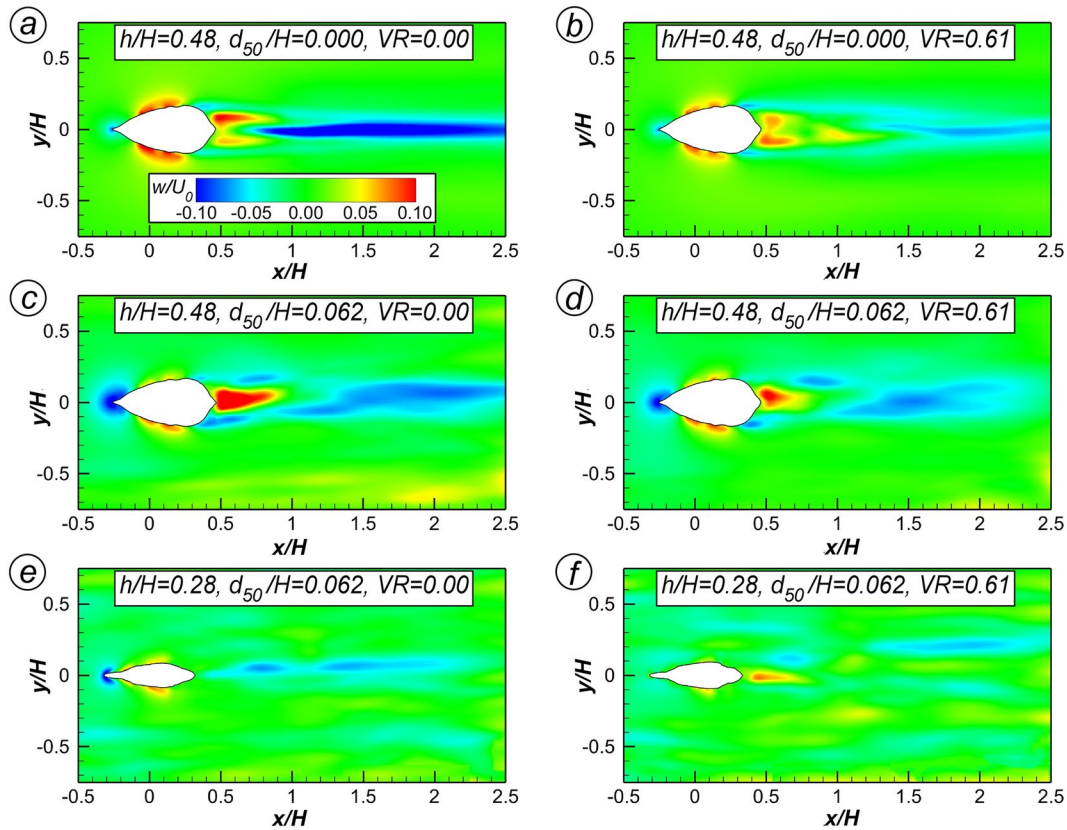

Figure 12. Mean vertical velocity, w/U_0, in the horizontal plane $z/H = 0.25$ for different simulations (a–f).

upwelling and downwelling flow motions and increases the asymmetry of these regions forming inside the near wake. At the front of the mussel, a fairly strong downflow is observed close to the front edge of the mussel, which is consistent with the formation of recirculating flow regions in Figure 9a ($d_{50}/H = 0.062$ case).

The effect of decreasing h/H in the rough bed ($d_{50}/H = 0.062$) simulations is to decrease the strength of the downwelling and upwelling motions in the near wake (e.g., compare corresponding cases with $h/H = 0.48$ in Figures 12c and 12d and $h/H = 0.28$ in Figures 12e and 12f). This result is consistent with the rapid loss of coherence of the tip vortices in the $h/H = 0.28$ simulations (Figures 10e and 10f). The formation of a small region of strong downwelling at the back of the mussel in the $h/H = 0.28$, $d_{50}/H = 0.062$, $VR = 0.61$ case is due to the presence of coherent counter-rotating base vortices at that location (see $x/H = 1$ section in Figure 10f). The increased level of mussel burial also reduces the strength of the adverse pressure gradients generated in front of the mussel, which explains the reduced downflow in the $h/H = 0.28$ cases (Figures 12e and 12f) compared to the corresponding $h/H = 0.48$ cases (Figures 12c and 12d).

The antisymmetric shedding mode is basically suppressed in the $h/D = 0.48$, $d_{50}/H = 0.00$, $VR = 0$ simulation due to the secondary flow generated by the main region of flow downwelling near the $y/H = 0$ plane (Figure 14a). The

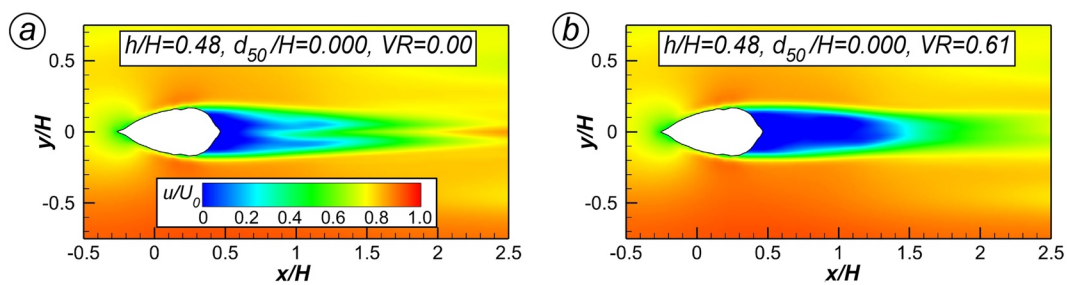

Figure 13. Mean streamwise velocity, u/U_0, in the horizontal plane $z/H = 0.25$ for different simulations (a, b).

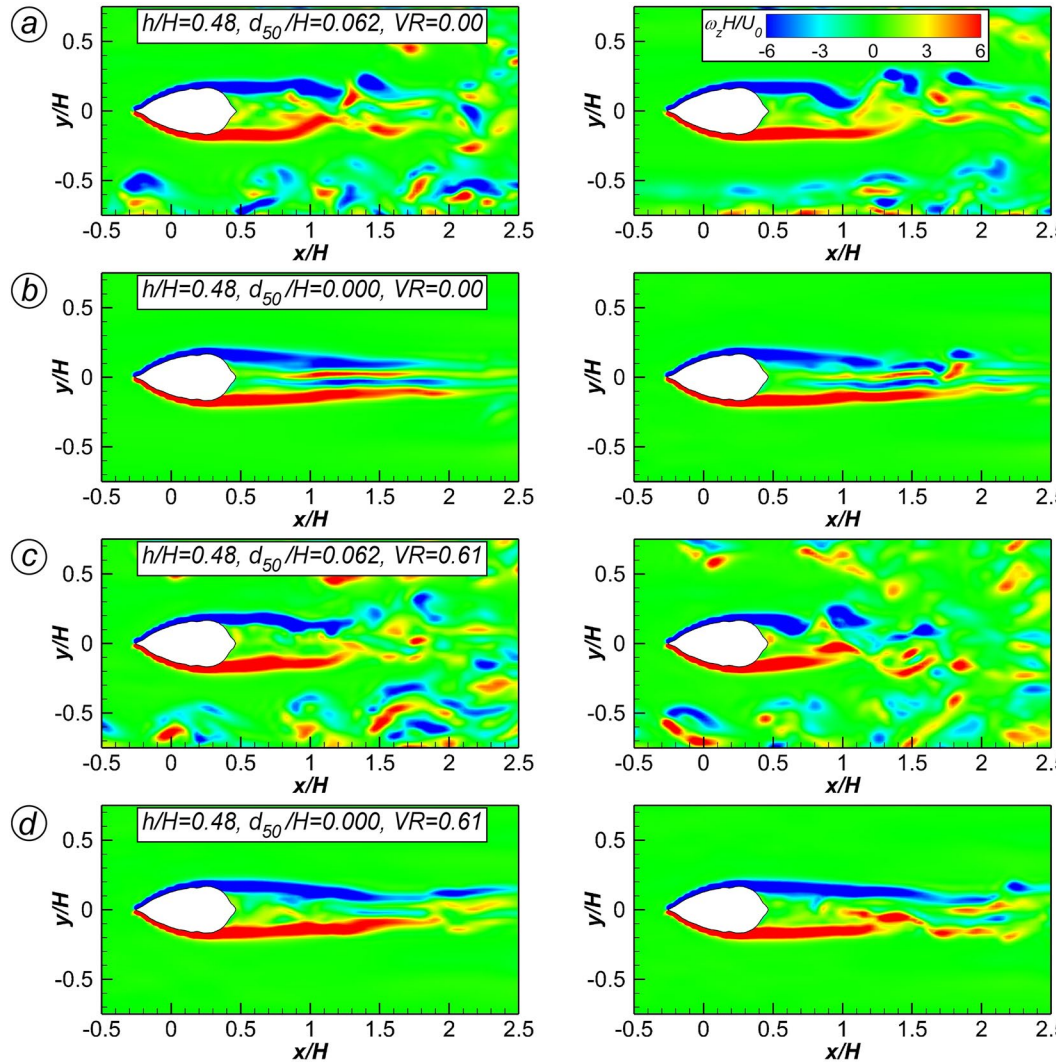

Figure 14. Instantaneous-flow, vertical vorticity, $\omega_z H/U_0$, in the horizontal plane $z/H = 0.25$ for different simulations (a–d). Left frames illustrate the symmetric wake shedding mode; right frames illustrate the anti-symmetric wake shedding mode (c–d) or the symmetric mode with a loss of symmetry for the eddies that detach from the downstream part of the separated shear layers (a–b).

secondary flow pushes the separated shear layers away from the symmetry plane, which impedes the natural oscillations of the separated shear layers that result in the generation of counter-rotating wake vortices. As the secondary flow reaches the separated shear layers it starts moving away from the bed, which explains the formation of two elongated patches of vorticity in between the symmetry plane and the two separated shear layers in Figure 14a. At times, there is some interaction between the two separated shear layers which results in the detachment and shedding of patches of vorticity from their downstream ends (e.g., see right frame in Figure 14a). The active filtering increases the interactions between the separated shear layers and eliminates the formation of the elongated patches of vorticity in between the symmetry plane and the separated shear layers (Figure 14b). However, these interactions do not result in shedding of counter-rotating wake vortices but rather in the shedding of eddies from the ends of the two separated shear layers that are interacting with each other as they are advected downstream.

For the smooth bed cases with and without filtering, the symmetric wake shedding mode remains the dominant one. This is different from cases considered by H. Wu, Constantinescu, and Zeng (2020) with a similar level of mussel burrowing where the antisymmetric mode was the dominant one. The shape of the exposed part of the mussel shell seems to control the type and coherence of the streamwise vortices forming in the wake, which in turn determines what shedding is more dominant in the wake.

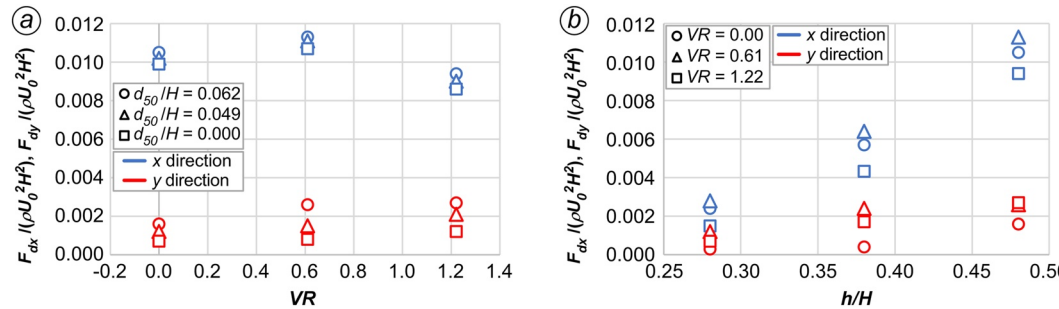

Figure 15. Non-dimensional drag forces, $F_{dx}/(\rho U_0{}^2H^2)$ and $F_{dy}/(\rho U_0{}^2H^2)$, in the simulations conducted with $h/H = 0.48$ and different values of the bed roughness, d_{50}/H, as a function of the velocity ratio VR (a), and for different values of VR, as a function of the level of mussel burrowing, h/H in the simulations conducted with $d_{50}/H = 0.062$ (b). Blue symbols refer to x-direction, red symbols to y-direction.

The increase in the bed roughness weakens the symmetric wake shedding mode and the secondary flow moving toward the two separated shear layers. The weakening of the secondary flow allows the antisymmetric wake shedding mode to grow and to gradually become dominant. In all the $h/H = 0.48$ simulations conducted with a bed roughness of $d_{50}/H = 0.062$, both modes are present. This is illustrated in Figures 14c and 14d for $VR = 0$ and $VR = 0.61$. While in the $VR = 0$ simulation the symmetric wake shedding mode is observed over about 70% of the simulation time, in the $VR = 0.61$ simulation the anti-symmetric wake shedding mode is stronger and is observed over 50%–55% of the simulation time. In the $VR = 1.22$ simulation, the symmetric shedding mode is observed over only 10% of the simulation time.

6. Drag Forces

The stability of the mussel and its capacity to avoid dislocation from the substrate are directly related to the drag forces acting on the emerged part of the shell. The total horizontal drag force, F_{dxy}, and its streamwise (F_{dx}) and lateral (F_{dy}) components are calculated by integrating the mean pressure acting on the emerged part of the shell, the contribution of the shear component being negligible. In the simulations with a rough bed, the drag forces are calculated in the $z > 0$ region to allow a direct comparison with the smooth bed cases. All drag forces are nondimensionalized using the water density, ρ, the section-averaged flow velocity, U_0, and the height of the mussel, H, which are constant for all simulations. These values are included in Table 1 along with values of the mean streamwise drag coefficient, $C_{dx}{}^{\mathrm{MEAN}}$, and the root-mean-square (RMS) of the drag coefficient fluctuations, $C_{dx}{}^{\mathrm{RMS}}$. The mean drag coefficient in the streamwise direction is defined as $C_{dx}{}^{\mathrm{MEAN}} = 2F_{dx}/(\rho U_0{}^2A_x)$, where A_x is the projected area of the emerged part of the mussel and varies with h/H.

For $h/H = 0.48$, the values of F_{dy} in Table 1 and Figure 15a can be as high as 30% of F_{dx} in the simulations conducted with a high bed roughness. This is due to the slight asymmetry of the two sides of the shell and to the near-bed flow asymmetry induced by the irregular bed surface. However, this percentage increases to 75% in the simulations conducted with a rough bed and a high degree of mussel burial (e.g., see for $h/H = 0.48$, $d_{50}/H = 0.062$, and $VR = 1.22$, see Table 1 and Figure 15b). Results in Figure 15 show that for constant bed roughness and level of mussel burrowing, F_{dy} is increasing monotonically with VR. By contrast, F_{dx} is increasing as the active filtering is turned on, peaks for $VR = 0.61$, and then decays for larger VR values. H. Wu, Constantinescu, and Zeng (2020) also observed an increase of F_{dx} with VR for $VR < 0.7$. It is likely that the trend reverses around $VR = 1$. For constant h/H (=0.48) and VR, both F_{dx} and F_{dy} increase with increasing bed roughness, but the rate of increase is higher for the lateral force (Figure 15a). Similar to the findings of H. Wu, Constantinescu, and Zeng (2020) for a mussel placed on a smooth bed and for constant VR, the streamwise drag force decreases with increasing level of mussel burial (Figure 15b); the spanwise drag force follows a similar trend, though its rate of decrease is lower compared to that of F_{dx}.

The trends in the variation of the streamwise drag coefficients with h/H, VR, and d_{50}/H are the same as the ones observed for F_{dx} (Figure 16). The peak value of $C_{dx}{}^{\mathrm{MEAN}}$ is around 0.17 which is about 50%–70% lower than those predicted by H. Wu, Constantinescu, and Zeng (2020). This difference is due to the much more streamlined shape of the frontal part of the mussel used in the present study. For varying level of mussel burial, the relative

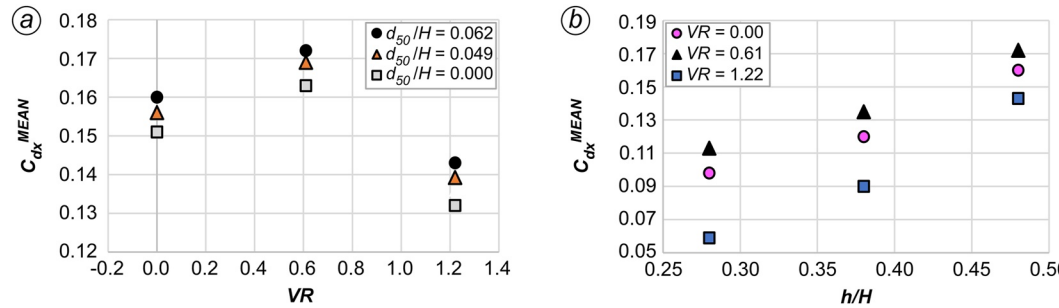

Figure 16. Mean drag coefficient, C_{dx}^{MEAN}, for the simulations conducted with $h/H = 0.48$ and different values of the bed roughness, d_{50}/H, as a function of the velocity ratio VR (a), and for different values of VR, as a function of the level of mussel burial, h/H, in the simulations conducted with $d_{50}/H = 0.062$ (b).

differences between the streamwise drag coefficients predicted for various values of h/H are smaller than the ones observed for the streamwise drag forces because the projected area decreases with increasing level of mussel burial. Still, C_{dx}^{MEAN} decreases by more than 50% as h/D decreases from 0.48 to 0.28 in the simulations conducted with $d_{50}/H = 0.062$ and $VR = 1.22$.

In the $h/H = 0.48$ simulations, the RMS of the drag coefficient fluctuations, C_{dx}^{RMS}, are typically less than 15% of C_{dx}^{MEAN} (Table 1). However, this percentage can increase to 40% in the simulations conducted with $h/H = 0.28$. For such cases, C_{dx}^{MEAN} is not a very good indicator of the capacity of the flow to dislocate the mussel and mussel stability calculations should be based on larger drag forces than those calculated using the mean drag coefficient.

7. Excurrent Siphon Jet

Mixing and dilution of the jet flow through the excurrent siphon are of particular interest for river ecology and water quality, as the water inhaled by the mussel is filtered of nutrients, organic matter and phytoplankton by the mussel organism before being released again into the water column (Haag, 2012; Monismith et al., 1990; Vaughn et al., 2004). The distribution and the availability of nutrients and phytoplankton in the flow are then directly connected with the dynamics of the excurrent siphon jet.

To study the jet dynamics and to quantify entrainment, a concentration $C_0 = 1$ is prescribed for the passive scalar introduced at the inlet of the pipe connecting to the excurrent siphon. Then, an "inverse concentration method" is used (Monismith et al., 1990; H. Wu, Constantinescu, & Zeng, 2020), such that $C = C_0$ represents the clean water filtered by the mussel, while $C = 0$ represents the water with high concentrations of nutrients and phytoplankton (Figure 17). The jet fluid is defined as the fluid with $C > 0.0001C_0$. In the region occupied by fluid from the excurrent siphon jet, the availability of nutrients is expected to be reduced (i.e., $C > 0$). The dynamics of the excurrent siphon jet is expected to be more complex than the one associated with a classical jet in cross flow because in the present set up the jet enters the channel some distance above the bed in a region where the incoming flow is diverted by the frontal part of the shell. Downstream of the mussel, the near-wake region contains streamwise oriented (tip) vortices, some of them induced by the emerged part of the shell. These vortices are not present in the well-studied case of a round vertical jet entering through the bottom of a flat-bed channel (Mahesh, 2013). Moreover, in the case of a rough bed and a relatively high level of mussel burial, the jet flow is expected to interact with the larger particles at the bed surface. This should result in an enhancement of local mixing and a more rapid dilution of the jet compared to cases with a larger h/H and/or a smooth bed.

The passive scalar concentration distributions in Figure 17 show that the base and/or tip vortices have a direct influence on the shape of the cross section of the excurrent siphon jet. In the smooth bed simulation with $h/H = 0.48$ and $VR = 0.61$ (Figure 17a), the elliptical cross section of the jet in the $x/H = 1$ section is due to the pair of base vortices that draws jet fluid away from the bed. In the $x/H = 3$ section, the base vortices occupy the same region as the upper part of the jet cross section ($z/H > 0.5$). The lower elongated region of high concentration forming near the symmetry ($y/H = 0$) plane is induced by the pair of counter-rotating tip vortices that draw some of the jet fluid toward the bed (Figures 11b and 17).

The distributions of the mean concentration in the corresponding rough bed case ($d_{50}/h = 0.062$) shown in Figure 17b are qualitatively similar to those observed in the smooth bed case. While the coherence of the base

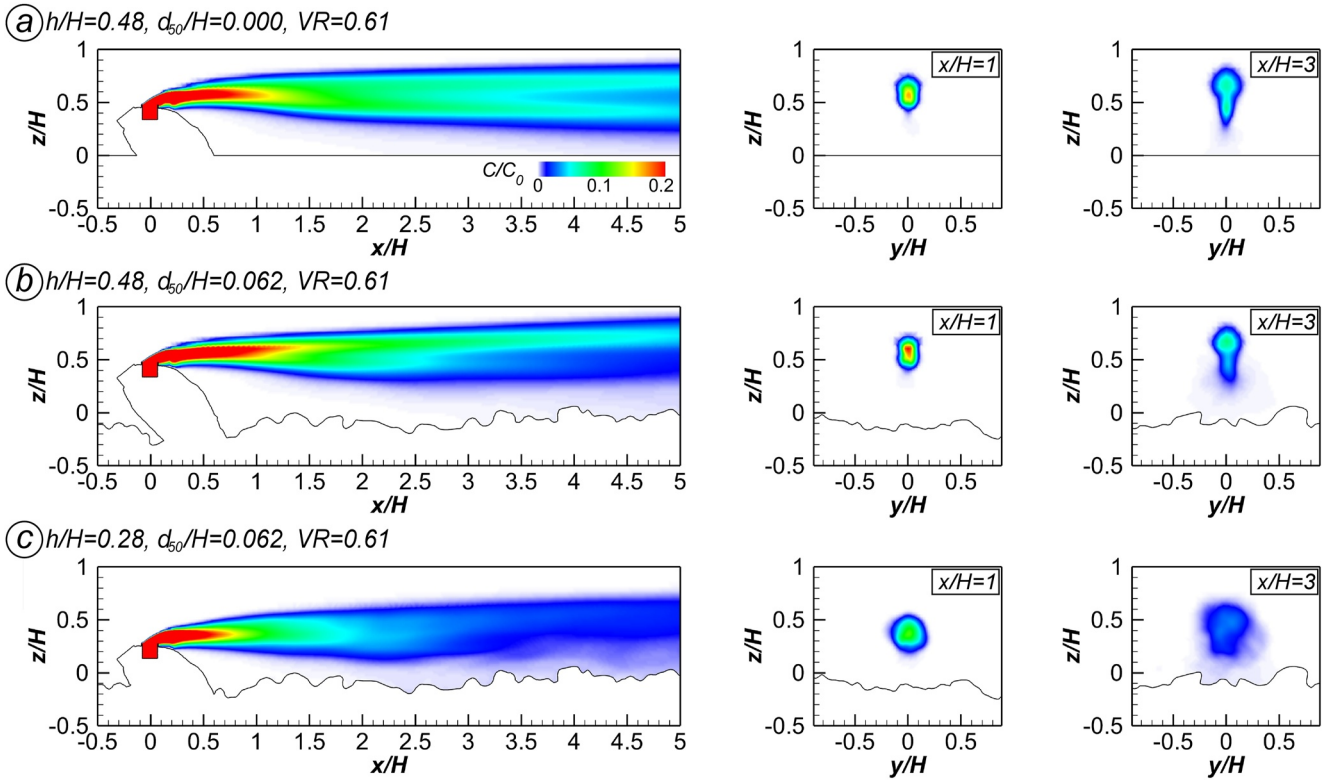

Figure 17. Mean concentration of the passive scalar, C/C_0 (values lower than 0.01 were blanked), for different simulations (a–c) in the $y/H = 0$ (left), $x/H = 1$ (center) and $x/H = 3$ (right) section planes.

and tip vortices is comparable in the $x/H = 1$ section in the two simulations, the coherence of the tip vortex is significantly lower in the rough bed simulation in the $x/H = 3$ section (Figures 10b and 10d). As a result, the length of the elongated region of relatively high concentration forming near the symmetry plane and the concentration levels inside this region are lower in the rough bed case.

The effect of increasing the level of mussel burial on the excurrent jet dynamics is illustrated by comparing the scalar concentration distributions in the $d_{50}/H = 0.062$, $VR = 0.61$ simulations conducted with $h/H = 0.48$ and $h/H = 0.28$ (see Figures 17b and 17c). Overall, the shape of the region of high concentration is much more circular and no elongated region of high concentration forms near the symmetry plane in the $x/H = 1$ and $x/H = 3$ sections. This is a direct consequence of the absence of tip vortices in the simulation conducted with $h/H = 0.28$ (Figure 10f). The other main difference is that the concentration levels decay much faster with increasing distance from the jet origin in the simulation with a larger level of mussel burial (Figures 17b and 17c). This effect is due the energetic eddies generated by the bed surface interacting with the lower part of the jet that is situated much close to the channel bed in the $h/H = 0.28$ simulation. These eddies are very effective at enhancing mixing between the jet fluid and the surrounding flow.

The effects of varying separately the bed roughness, the discharge through the excurrent siphon and the level of mussel burial on the jet dynamics are illustrated in a quantitative way in Figures 18 and 19. A measure of the jet dilution is the streamwise variation of the maximum passive scalar concentration in cross sections perpendicular to the axis of the jet (Figure 18). The variation of the volumetric flux of the jet, Q_j, scaled by the volumetric flux out of the excurrent siphon, Q_{j0}, measures entrainment into the jet and it is plotted in Figure 19.

For cases with a relatively low level of mussel burial (e.g., for $h/H = 0.48$), the streamwise decay of the maximum concentration in the jet cross section is fairly independent of the bed roughness. Slightly lower values of C_{MAX}/C_0 are predicted for $x/H > 6$ in the simulation with the highest bed roughness (Figure 18a). By contrast, the volumetric flux of the jet increases monotonically with increasing bed roughness. For example, the volumetric flux doubles in the $d_{50}/H = 0.062$ simulation compared to the corresponding smooth bed simulation around $x/H = 9$

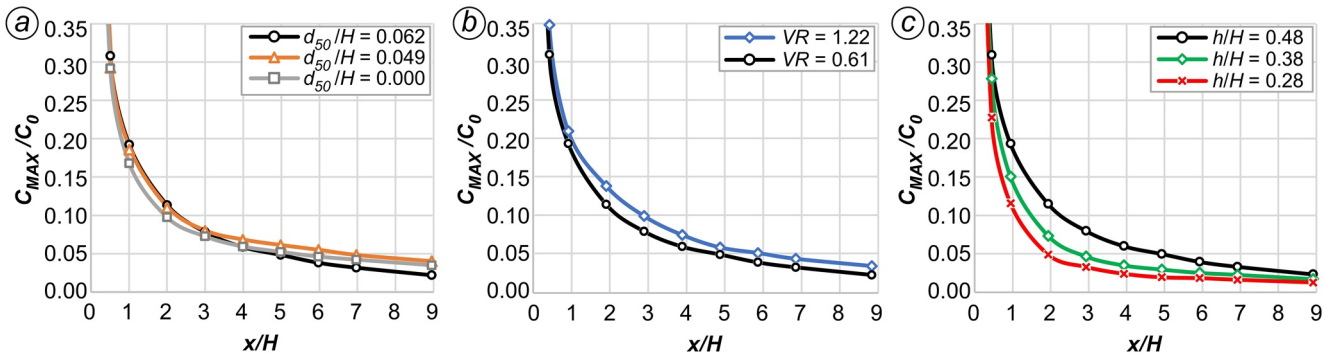

Figure 18. Non-dimensional peak scalar concentration, C_{MAX}/C_0, inside the excurrent jet. (a) Effect of d_{50}/H ($VR = 0.61$, $h/H = 0.48$); (b) effect of VR ($d_{50}/H = 0.062$, $h/H = 0.48$); (c) effect of h/H ($d_{50}/H = 0.062$, $VR = 0.61$).

(Figure 19a). This increase is induced by eddies generated at the bed surface that interact with the lower part of the jet fluid.

The mean excurrent-siphon velocities in the simulations conducted with $VR = 0.61$ and $VR = 1.22$ are 0.1 and 0.2 m/s, respectively. The jet has a larger initial momentum in simulations conducted with higher values of VR. Consequently, the excurrent siphon jet will penetrate up to higher elevations with respect to the excurrent siphon location and the streamwise distance needed by the jet to align with the streamwise direction will be larger in simulations conducted with a larger VR. Based on comparing $h/H = 0.48$, $d_{50}/H = 0.062$ simulations with $VR = 0.61$ and $VR = 1.22$, despite the marked differences in the trajectories of the excurrent siphon jet in the two simulations, one can conclude that the effect of increasing the excurrent jet discharge on the streamwise variation of C_{MAX}/C_0 is fairly negligible (Figure 18). This is because the jet is situated relatively far away from the bed in both simulations. Interestingly, the rate of increase of the volumetric discharge is larger in the simulation conducted with a smaller excurrent jet discharge (Figure 19b). The main reason for this difference is that the jet is situated closer to the bed surface in the $VR = 0.61$ simulation. The other reason is that the growth of flow instabilities near the jet boundaries and mixing are driven by the mean shear between the velocity inside the core of the jet and the velocity in the surrounding flow. One expects this effect to be the lowest for cases with $VR \simeq 1$ where the excurrent jet velocity is close to the mean velocity in the flow surrounding the jet.

Increasing the level of mussel burial in the rough bed simulations conducted with $d_{50}/H = 0.062$ and $VR = 0.61$ results in larger rates of decay for C_{MAX}/C_0 until $x/H = 2$ (Figure 18c). The trend then reverses such that the maximum concentration values are fairly close by $x/H = 8$. The decrease of C_{MAX}/C_0 with decreasing h/H over the upstream part of the jet is due to the strong mixing induced by the eddies generated by the bed surface. As h/H decays, these eddies will get closer to the lower boundary of the jet. However, once the jet expands enough such that it touches the bed, this effect will be negligible. Somewhat surprisingly, the streamwise variation of the volumetric flux is nearly independent of the level of mussel burial in the three simulations compared in Figure 19c. This is likely the result of two competing effects. On one hand, the cross section of the jet at a given

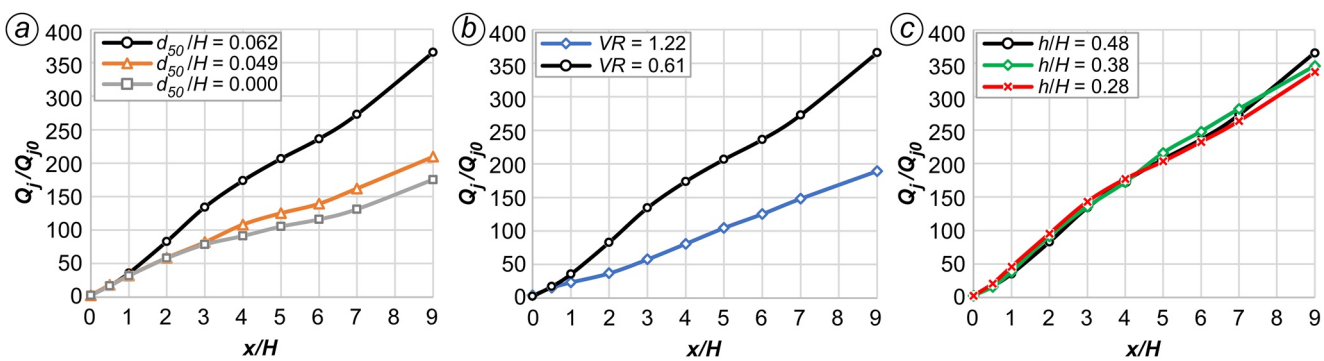

Figure 19. Non-dimensional volumetric flux, Q_j/Q_{j0}, of the excurrent siphon jet. (a) Effect of d_{50}/H ($VR = 0.61$, $h/H = 0.48$); (b) effect of VR ($d_{50}/H = 0.062$, $h/H = 0.48$); (c) effect of h/H ($d_{50}/H = 0.062$, $VR = 0.61$).

streamwise location increases with decreasing h/H due to stronger mixing taking part around the lower boundary of the jet. On the other hand, the jet will be situated closer to the bed where the streamwise flow velocities are lower compared to cases with higher h/H.

8. Discussion and Conclusions

The present study focused on flow and turbulence structure around a partially-burrowed mussel placed on a rough bed aligned with the incoming flow. The bed roughness was resolved in the eddy-resolving simulations and corresponded to a gravel bed. In this respect, the present study extends the findings of H. Wu, Constantinescu, and Zeng (2020) who focused on a similar configuration where a mussel of a different species was placed on a horizontal smooth bed. Given that mussel beds are common in sand and gravel bed rivers, understanding the effects of the bed roughness for a relevant range of values of the ratio, h/d_{50}, between the emerged part of the mussel and the average height of the particles present at the bed surface is of particular importance. One should note that as h/d_{50} decreases toward unity, the mussel will just behave as a bed particle.

The present study showed that the vortical structure of the flow, the coherence and the dynamics of these vortices forming around the mussel are significantly affected by the shape of the emerged part of the mussel and by its orientation. The shape of the shell affects the capacity of these vortices to increase the bed shear stress and to induce local scour in front and behind the mussel. The presence of a rough bed that mimics a gravel bed was found to induce not only quantitative but also qualitative changes in the vortical structure of the flow, with the antisymmetric shedding mode gradually becoming dominant with increasing bed roughness. This change in the wake structure happens because the irregular bed surface breaks the symmetry of the wake flow and reduces the coherence of the tip vortices. Another important finding was that if the filtering ratio VR is kept constant, the streamwise drag force coefficient and the volumetric flux of the excurrent jet increase with increasing bed roughness. The presence of a rough bed that mimics a gravel bed was also shown to decrease mussel stability, as the drag forces were found to increase with increasing bed roughness, but to increase the dilution and mixing of the exhaling siphon jet.

Future research will investigate to what extent the present findings on how the geometry of the mussel and the bed characteristics affect flow and transport processes around an isolated, partially-burrowed mussel apply for clusters of mussels and large array of mussels (mussel beds) where mussel-to-mussel interactions are important. The present work considered only relatively high submergence ratios and impermeable substrates. Further research is needed to understand how mussel stability, drag forces and wake structure change for cases when the mussels start interacting with the free surface. Calculations with a permeable substrate will allow understanding the role played by the hyporheic flow and how particulates present in the incoming flow settle into the substrate.

Data Availability Statement

The data can be accessed online at: https://researchdata.cab.unipd.it/834/, https://doi.org/10.25430/researchdata.cab.unipd.it.00000771.

Acknowledgments

This study was supported by Italian National Research Programme PRIN 2017, with the project "*IntEractions between hydrodyNamics flows and bioTic communities in fluvial Ecosystems: advancement in dischaRge monitoring and understanding of Processes Relevant for ecosystem sustaInability by the development of novel technologies with fIeld observatioNs and laboratory testinG (ENTERPRISING)*." The CINECA award HP10C0AGT9 under the ISCRA initiative is acknowledged for the availability of high-performance computing resources and support. Nina Benistati, Ph.D. student at the University of Palermo, is gratefully acknowledged for collecting the experimental data used in the present work. Nicoletta Riccardi, permanent researcher at CNR–IRSA, is gratefully acknowledged for providing the mussel used in the experiments and valuable information on mussel anatomy and filtering activity. T. Lazzarin is sponsored by a PhD scholarship funded by the *CARIPARO* Foundation, and by a scholarship provided by the A. Gini Foundation for his research period at IIHR. G. Constantinescu and H. Wu acknowledge partial support from the EAR Hydrologic Science Program of the US National Science Foundation under Grant 1659518. Open Access Funding provided by Universita degli Studi di Padova within the CRUI-CARE Agreement.

References

Blettler, M., Sukhodolov, A., & Tockner, K. (2010). Hydraulic conditions over bed forms control the benthic fauna distribution in a lowland river (Spree River, Germany). In A. Dittrich, K. Koll, J. Aberle, & P. Geisenhainer (Eds.), *Proceeding of river flow 2010, 1463–1468*. Bundesanstalt fur Wasserbau.

Bunt, C. M., Maclsaac, H. J., & Sprules, W. G. (1993). Pumping rates and projected filtering impacts of Juvenile Zebra mussels (*Dreissena polymorpha*) in Western Lake Erie. *Canadian Journal of Fisheries and Aquatic Sciences*, *50*(5), 1017–1022. https://doi.org/10.1139/f93-117

Carrivick, J. L., Smith, M. W., & Quincey, D. J. (2016). *Structure from motion in geosciences*. John Wiley & Sons, Ltd. https://doi.org/10.1002/9781118895818

Chang, K., & Constantinescu, G. (2013). Coherent structures in flow over two-dimensional dunes. *Water Resources Research*, *49*(5), 2446–2460. https://doi.org/10.1002/wrcr.20239

Chang, K., Constantinescu, G., & Park, S.-O. (2007a). Assessment of predictive capabilities of detached eddy simulation to simulate flow and mass transport past open cavities. *Journal of Fluids Engineering*, *129*(11), 1372–1383. https://doi.org/10.1115/1.2786529

Chang, K., Constantinescu, G., & Park, S.-O. (2007b). Purging of a neutrally buoyant or a dense miscible contaminant from a rectangular cavity. II: Case of an incoming fully turbulent overflow. *Journal of Hydraulic Engineering*, *133*(4), 373–385. https://doi.org/10.1061/(ASCE)0733-9429(2007)133:4(373)

Chang, W.-Y., Constantinescu, G., & Tsai, W.-F. (2020). Effect of array submergence on flow and coherent structures through and around a circular array of rigid vertical cylinders. *Physics of Fluids*, *32*(3), 035110. https://doi.org/10.1063/1.5138604

Chen, Y., DiBiase, R. A., McCarroll, N., & Liu, X. (2019). Quantifying flow resistance in mountain streams using computational fluid dynamics modeling over structure-from-motion photogrammetry-derived microtopography. *Earth Surface Processes and Landforms*, *44*(10), 1973–1987. https://doi.org/10.1002/esp.4624

Constantinescu, G. (2014). LE of shallow mixing interfaces: A review. *Environmental Fluid Mechanics*, *14*(5), 971–996. https://doi.org/10.1007/s10652-013-9303-6

Constantinescu, G., Chapelet, M., & Squires, K. (2003). Turbulence modeling applied to flow over a sphere. *AIAA Journal*, *41*(9), 1733–1742. https://doi.org/10.2514/2.7291

Constantinescu, G., Miyawaki, S., & Liao, Q. (2013). Flow and turbulence structure past a cluster of freshwater mussels. *Journal of Hydraulic Engineering*, *139*(4), 347–358. https://doi.org/10.1061/(ASCE)HY.1943-7900.0000692

Constantinescu, G. S., & Squires, K. D. (2003). LES and DES investigations of turbulent flow over a sphere at Re = 10,000. *Flow, Turbulence and Combustion*, *70*(1), 267–298. https://doi.org/10.1023/B:APPL.0000004937.34078.71

Crimaldi, J. P., Thompson, J. K., Rosman, J. H., Lowe, R. J., & Koseff, J. R. (2002). Hydrodynamics of larval settlement: The influence of turbulent stress events at potential recruitment sites. *Limnology & Oceanography*, *47*(4), 1137–1151. https://doi.org/10.4319/lo.2002.47.4.1137

Di Maio, J., & Corkum, L. D. (1997). Patterns of orientation in unionids as a function of rivers with differing hydrological variability. *Journal of Molluscan Studies*, *63*(4), 531–539. https://doi.org/10.1093/mollus/63.4.531

Doucet, C. V., Labaj, A. L., & Kurek, J. (2021). Microfiber content in freshwater mussels from rural tributaries of the saint John river, Canada. *Water, Air, & Soil Pollution*, *232*(1), 32. https://doi.org/10.1007/s11270-020-04958-4

Engelhardt, C., Krüger, A., Sukhodolov, A., & Nicklisch, A. (2004). A study of phytoplankton spatial distributions, flow structure and characteristics of mixing in a river reach with groynes. *Journal of Plankton Research*, *26*(11), 1351–1366. https://doi.org/10.1093/plankt/fbh125

Ferreira-Rodríguez, N., Akiyama, Y. B., Aksenova, O. V., Araujo, R., Christopher Barnhart, M., Bespalaya, Y. V., et al. (2019). Research priorities for freshwater mussel conservation assessment. *Biological Conservation*, *231*, 77–87. https://doi.org/10.1016/j.biocon.2019.01.002

Froufe, E., Lopes-Lima, M., Riccardi, N., Zaccara, S., Vanetti, I., Lajtner, J., et al. (2017). Lifting the curtain on the freshwater mussel diversity of the Italian Peninsula and Croatian Adriatic coast. *Biodiversity & Conservation*, *26*(14), 3255–3274. https://doi.org/10.1007/s10531-017-1403-z

Gutiérrez, J. L., Jones, C. G., Strayer, D. L., & Iribarne, O. O. (2003). Mollusks as ecosystem engineers: The role of shell production in aquatic habitats. *Oikos*, *101*(1), 79–90. https://doi.org/10.1034/j.1600-0706.2003.12322.x

Haag, W. R. (2012). *North American freshwater mussels: Natural history, ecology, and conservation*. Cambridge University Press.

Hajimirzaie, S. M., & Buchholz, J. H. J. (2013). Flow dynamics in the wakes of low-aspect-ratio wall-mounted obstacles. *Experiments in Fluids*, *54*(11), 1616. https://doi.org/10.1007/s00348-013-1616-1

Hajimirzaie, S. M., Wojcik, C. J., & Buchholz, J. H. J. (2012). The role of shape and relative submergence on the structure of wakes of low-aspect-ratio wall-mounted bodies. *Experiments in Fluids*, *53*(6), 1943–1962. https://doi.org/10.1007/s00348-012-1406-1

Hajisafarali, M., Aaltonen, S., Pulkkinen, K., & Taskinen, J. (2022). Does the freshwater mussel Anodonta anatina remove the fish pathogen Flavobacterium columnare from water? *Hydrobiologia*, *849*(4), 1067–1081. https://doi.org/10.1007/s10750-021-04769-6

Heinz, S. (2020). A review of hybrid RANS-LES methods for turbulent flows: Concepts and applications. *Progress in Aerospace Sciences*, *114*, 100597. https://doi.org/10.1016/j.paerosci.2019.100597

Horna-Munoz, D., & Constantinescu, G. (2018). A fully 3-D numerical model to predict flood wave propagation and assess efficiency of flood protection measures. *Advances in Water Resources*, *122*, 148–165. https://doi.org/10.1016/j.advwatres.2018.10.014

Howard, J. K., & Cufey, K. M. (2006). The functional role of native freshwater mussels in the fluvial benthic environment. *Freshwater Biology*, *51*(3), 460–474. https://doi.org/10.1111/j.1365-2427.2005.01507.x

Keylock, C. J., Constantinescu, G., & Hardy, R. J. (2012). The application of computational fluid dynamics to natural river channels: Eddy resolving versus mean flow approaches. *Geomorphology*, *179*, 1–20. https://doi.org/10.1016/j.geomorph.2012.09.006

Keylock, C. J., Hardy, R. J., Parsons, D. R., Ferguson, R. I., Lane, S. N., & Richards, K. S. (2005). The theoretical foundations and potential for large-eddy simulation (LES) in fluvial geomorphic and sedimentological research. *Earth-Science Reviews*, *71*(3), 271–304. https://doi.org/10.1016/j.earscirev.2005.03.001

Kirkil, G., & Constantinescu, G. (2009). Nature of flow and turbulence structure around an in-stream vertical plate in a shallow channel and the implications for sediment erosion. *Water Resources Research*, *45*(6), W06412. https://doi.org/10.1029/2008WR007363

Koken, M., & Constantinescu, G. (2009). An investigation of the dynamics of coherent structures in a turbulent channel flow with a vertical sidewall obstruction. *Physics of Fluids*, *21*(8), 085104. https://doi.org/10.1063/1.3207859

Kreeger, D. A., Gatenby, C. M., & Bergstrom, P. W. (2018). Restoration potential of several native species of Bivalve molluscs for water quality improvement in mid-Atlantic watersheds. *Journal of Shellfish Research*, *37*(5), 1121–1157. https://doi.org/10.2983/035.037.0524

Kryger, J., & Riisgård, H. U. (1988). Filtration rate capacities in 6 species of European freshwater bivalves. *Oecologia*, *77*(1), 34–38. https://doi.org/10.1007/BF00380921

Kumar, S. S., Kozarek, J., Hornbach, D., Hondzo, M., & Hong, J. (2019). Experimental investigation of turbulent flow over live mussels. *Environmental Fluid Mechanics*, *19*(6), 1417–1430. https://doi.org/10.1007/s10652-019-09664-2

Lacey, R. W. J., & Rennie, C. D. (2012). Laboratory investigation of turbulent flow structure around a bed-mounted cube at multiple flow stages. *Journal of Hydraulic Engineering*, *138*(1), 71–84. https://doi.org/10.1061/(ASCE)HY.1943-7900.0000476

Lazzarin, T., Viero, D. P., Defina, A., & Cozzolino, L. (2023). Flow under vertical sluice gates: Flow stability at large gate opening and disambiguation of partial dam-break multiple solutions. *Physics of Fluids*, *35*(2), 024114. https://doi.org/10.1063/5.0131953

Lohrer, A. M., Thrush, S. F., & Gibbs, M. M. (2004). Bioturbators enhance ecosystem function through complex biogeochemical interactions. *Nature*, *431*(7012), 1092–1095. https://doi.org/10.1038/nature03042

Lopes-Lima, M., Sousa, R., Geist, J., Aldridge, D. C., Araujo, R., Bergengren, J., et al. (2017). Conservation status of freshwater mussels in Europe: State of the art and future challenges. *Biological Reviews*, *92*(1), 572–607. https://doi.org/10.1111/brv.12244

Lopez, J. W., DuBose, T. P., Franzen, A. J., Atkinson, C. L., & Vaughn, C. C. (2022). Long-term monitoring shows that drought sensitivity and riparian land use change coincide with freshwater mussel declines. *Aquatic Conservation: Marine and Freshwater Ecosystems*, *32*(10), 1571–1583. https://doi.org/10.1002/aqc.3884

Lopez, J. W., & Vaughn, C. C. (2021). A review and evaluation of the effects of hydrodynamic variables on freshwater mussel communities. *Freshwater Biology*, *66*(9), 1665–1679. https://doi.org/10.1111/fwb.13784

Lydeard, C., Cowie, R. H., Ponder, W. F., Bogan, A. E., Bouchet, P., Clark, S. A., et al. (2004). The global decline of nonmarine mollusks. *BioScience*, *54*(4), 321–330. https://doi.org/10.1641/0006-3568(2004)054[0321:TGDONM]2.0.CO;2

Mahesh, K. (2013). The interaction of jets with crossflow. *Annual Review of Fluid Mechanics*, *45*(1), 379–407. https://doi.org/10.1146/annurev-fluid-120710-101115

Marion, A., Nikora, V., Puijalon, S., Bouma, T., Koll, K., Ballio, F., et al. (2014). Aquatic interfaces: A hydrodynamic and ecological perspective. *Journal of Hydraulic Research*, *52*(6), 744–758. https://doi.org/10.1080/00221686.2014.968887

Marrone, F., Gianbattista, N., Cianfanelli, S., Govedic, M., Barra, S., Arculeo, M., & Bodon, M. (2019). Diversity and taxonomy of the genus *Unio Philipsson* in Italy, with the designation of a neotype for *Unio elongatulus* C. Pfeiffer (Mollusca, Bivalvia, Unionidae). *Zootaxa*, *4545*(3), 339–374. https://doi.org/10.11646/zootaxa.4545.3.2

McCoy, A., Constantinescu, G., & Weber, L. (2007). A numerical investigation of coherent structures and mass exchange processes in channel flow with two lateral submerged groynes. *Water Resources Research*, *43*(5), 1–26. https://doi.org/10.1029/2006WR005267

Menter, F. R. (1994). Two-equation eddy-viscosity turbulence models for engineering applications. *AIAA Journal*, *32*(8), 1598–1605. https://doi.org/10.2514/3.12149

Menter, F. R., Hüppe, A., Matyushenko, A., & Kolmogorov, D. (2021). An overview of hybrid RANS–LES models developed for industrial CFD. *Applied Sciences*, *11*(6), 2459. https://doi.org/10.3390/app11062459

Menter, F. R., Kuntz, M., & Langtry, R. (2003). Ten years of industrial experience with the SST turbulence model. *Turbulence, Heat and Mass Transfer*, *4*(1), 625–632.

Modesto, V., Tosato, L., Pilbala, A., Benistati, N., Fraccarollo, L., Termini, D., et al. (2023). Mussel behaviour as a tool to measure the impact of hydraulic stressors. *Hydrobiologia*, *850*(4), 807–820. https://doi.org/10.1007/s10750-022-05126-x

Monismith, S. G., Koseff, J. R., Thompson, J. K., O'Riordan, C. A., & Nepf, H. M. (1990). A study of model bivalve siphonal currents. *Limnology & Oceanography*, *35*(3), 680–696. https://doi.org/10.4319/lo.1990.35.3.0680

Morales, Y., Weber, L. J., Mynett, A. E., & Newton, T. J. (2006). Effects of substrate and hydrodynamic conditions on the formation of mussel beds in a large river. *Journal of the North American Benthological Society*, *25*(3), 664–676. https://doi.org/10.1899/0887-3593(2006)25[664:EOSAHC]2.0.CO;2

Nakato, T., Christensen, J., & Schonhoff, B. (2007). Freshwater mussel survey in pool 16, the Mississippi river, near Fairport, Iowa: Rm 463.5-Rm 464.1, approximately. In *IIHR technical report 464*. The University of Iowa, IIHR-Hydroscience.

Newton, T. J., Woolnough, D. A., & Strayer, D. L. (2008). Using landscape ecology to understand and manage freshwater mussel populations. *Journal of the North American Benthological Society*, *27*(2), 424–439. https://doi.org/10.1899/07-076.1

Nikora, V. (2010). Hydrodynamics of aquatic ecosystems: An interface between ecology, biomechanics and environmental fluid mechanics. *River Research and Applications*, *26*(4), 367–384. https://doi.org/10.1002/rra.1291

Nishizaki, M., & Ackerman, J. D. (2017). Mussels blow rings: Jet behavior affects local mixing. *Limnology & Oceanography*, *62*(1), 125–136. https://doi.org/10.1002/lno.10380

O'Riordan, C. A., Monismith, S. G., & Koseff, J. R. (1995). The effect of bivalve excurrent jet dynamics on mass transfer in a benthic boundary layer. *Limnology & Oceanography*, *40*(2), 330–344. https://doi.org/10.4319/lo.1995.40.2.0330

Papanicolaou, A. N., Tsakiris, A. G., Wyssmann, M. A., & Kramer, C. M. (2018). Boulder array effects on bedload pulses and depositional patches. *Journal of Geophysical Research: Earth Surface*, *123*(11), 2925–2953. https://doi.org/10.1029/2018JF004753

Patankar, S. V., & Spalding, D. B. (1972). A calculation procedure for heat, mass and momentum transfer in three-dimensional parabolic flows. *International Journal of Heat and Mass Transfer*, *15*(10), 1787–1806. https://doi.org/10.1016/0017-9310(72)90054-3

Perles, S. J., Christian, A. D., & Berg, D. J. (2003). Vertical migration, orientation, aggregation, and fecundity of the freshwater mussel *Lampsilis siliquoidea*. *Ohio Journal of Science*, *103*(4), 73–78.

Qin, J., Pan, H., Rahman, M. M., Rian, X., & Zhu, Z. (2021). Introducing compressibility with SIMPLE algorithm. *Mathematics and Computers in Simulation*, *180*, 328–353. https://doi.org/10.1016/j.matcom.2020.09.010

Rehmann, C. R., Stoeckel, J. A., & Schneider, D. W. (2003). Effect of turbulence on the mortality of zebra mussel veligers. *Canadian Journal of Zoology*, *81*(6), 1063–1069. https://doi.org/10.1139/z03-090

Sadeque, M. A. F., Rajaratnam, N., & Loewen, M. R. (2008). Flow around cylinders in open channels. *Journal of Engineering Mechanics*, *134*(1), 60–71. https://doi.org/10.1061/(ASCE)0733-9399(2008)134:1(60)

Sadeque, M. A. F., Rajaratnam, N., & Loewen, M. R. (2009). Shallow turbulent wakes behind bed-mounted cylinders in open channels. *Journal of Hydraulic Research*, *47*(6), 727–743. https://doi.org/10.3826/jhr.2009.3464

Sansom, B. J., Atkinson, J. F., & Bennett, S. J. (2018). Modulation of near-bed hydrodynamics by freshwater mussels in an experimental channel. *Hydrobiologia*, *810*(1), 449–463. https://doi.org/10.1007/s10750-017-3172-9

Shamloo, H., Rajaratnam, N., & Katopodis, C. (2001). Hydraulics of simple habitat structures. *Journal of Hydraulic Research*, *39*(4), 351–366. https://doi.org/10.1080/00221680109499840

Singh, S. K., Raushan, P. K., & Debnath, K. (2019). Role of multiple flow stages over submerged structure. *Ocean Engineering*, *181*, 59–70. https://doi.org/10.1016/j.oceaneng.2019.03.048

Strayer, D. L. (1999). Use of flow refuges by unionid mussels in rivers. *Journal of the North American Benthological Society*, *18*(4), 468–476. https://doi.org/10.2307/1468379

Strayer, D. L., Downing, J. A., Haag, W. R., King, T. L., Layzer, J. B., Newton, T. J., & Nichols, J. S. (2004). Changing perspectives on pearly mussels, North America's most imperiled animals. *BioScience*, *54*(5), 429–439. https://doi.org/10.1641/0006-3568(2004)054[0429:CPOPMN]2.0.CO;2

Vaughn, C. C., Gido, K. B., & Spooner, D. E. (2004). Ecosystem processes performed by unionid mussels in stream mesocosms: Species roles and effects of abundance. *Hydrobiologia*, *527*(1), 35–47. https://doi.org/10.1023/B:HYDR.0000043180.30420.00

Vaughn, C. C., Nichols, S. J., & Spooner, D. E. (2008). Community and foodweb ecology of freshwater mussels. *Journal of the North American Benthological Society*, *27*(2), 409–423. https://doi.org/10.1899/07-058.1

Wu, H., & Constantinescu, G. (2022). Effect of angle of attack on flow past a partially-burrowed, isolated freshwater mussel. *Advances in Water Resources*, *168*, 104302. https://doi.org/10.1016/j.advwatres.2022.104302

Wu, H., Constantinescu, G., & Zeng, J. (2020). Flow and entrainment mechanisms around a freshwater mussel aligned with the incoming flow. *Water Resources Research*, *56*(9), e2020WR027983. https://doi.org/10.1029/2020WR027983

Wu, H., Zeng, J., & Constantinescu, G. (2021). A multi-parameter design formula for riprap size selection at wing-wall abutments. *Journal of Hydraulic Research*, *59*(4), 651–661. https://doi.org/10.1080/00221686.2020.1818310

Wu, P., Horna-Munoz, D., Constantinescu, G., & Qian, Z. (2020). Two-phase flow DES and URANS simulations of pump-intake bay vortices. *Journal of Hydraulic Research*, *58*(1), 120–132. https://doi.org/10.1080/00221686.2018.1555552

Xu, Q., Li, R., & Xu, M. (2022). High-performance implementation of parallel semi-implicit method for pressure linked equations solver on CPU+ GPU platform. *International Journal of Heat and Mass Transfer*, *182*, 121976. https://doi.org/10.1016/j.ijheatmasstransfer.2021.121976

Zigler, S. J., Newton, T. J., Steuer, J. J., Bartsch, M. R., & Sauer, J. S. (2008). Importance of physical and hydraulic characteristics to unionid mussels: A retrospective analysis in a reach of large river. *Hydrobiologia*, *598*(1), 343–360. https://doi.org/10.1007/s10750-007-9167-1